

# High-Order Central ENO Finite-Volume Scheme for MHD on Three-Dimensional Cubed-Sphere Grids

L. Ivan\*, A. Susanto\*, H. De Sterck\* and C.P.T. Groth\*\*  
Corresponding author: livan@math.uwaterloo.ca

\* Department of Applied Mathematics, University of Waterloo, Waterloo, ON, Canada.

\*\* University of Toronto Institute for Aerospace Studies, Toronto, ON, Canada.

**Abstract:** A high-order central essentially non-oscillatory (CENO) finite-volume scheme is developed for the compressible ideal magnetohydrodynamics (MHD) equations solved on three-dimensional (3D) cubed-sphere grids. The proposed formulation is an extension to 3D geometries of a recent high-order MHD CENO scheme developed on two-dimensional (2D) grids. The main technical challenge in extending the 2D method to 3D cubed-sphere grids is to properly handle the nonplanar cell faces that arise in cubed-sphere grids. This difficulty is solved by considering general hexahedral cells with trilinear faces, which allow us to compute fluxes, areas and volumes with high-order accuracy by transforming to a reference cubic cell. The 3D CENO scheme is implemented within a flexible multi-block cubed-sphere grid framework to fourth-order accuracy, resulting in a high-order solution method for cubed-sphere grids with unique capabilities in terms of adaptive refinement and parallel scalability. The high-order method is applicable to the solution of general hyperbolic conservation laws with, in principle, arbitrary order. The CENO scheme is based on a hybrid solution reconstruction procedure that provides high-order accuracy in smooth regions, even for smooth extrema, and non-oscillatory transitions at discontinuities. The scheme is applied herein to MHD in combination with a GLM divergence correction technique to control the solenoidal condition for the magnetic field while preserving the high-order accuracy of the numerical procedure. The cubed-sphere simulation framework features a flexible design based on a genuine multi-block implementation, leading to high-order accuracy, flux calculation, adaptivity and parallelism that are fully transparent to the boundaries between the six sectors of the cubed-sphere grid. The proposed 3D MHD CENO scheme is shown to achieve uniform fourth-order accuracy on cubed-sphere grids. Parallel domain partitioning and grid adaptivity are achieved on the 3D cubed-sphere grids using a hierarchical block-based division strategy with blocks of equal size. Numerical results to demonstrate the high-order accuracy, robustness and capability of the proposed high-order framework are presented and discussed for several test problems.

*Keywords:* Magnetohydrodynamics, High-Order Schemes, Cubed-Sphere Grids.

## 1 Introduction and Motivation

High-performance computational methods for numerically solving conservation laws in domains between two concentric spheres are highly desirable for computations of global physical processes associated with geophysical and celestial bodies and the intervening space, which arise in fields as diverse as space physics, astrophysics, climate and weather modelling, and geophysics. For example, accurate capturing of detailed flow features in space-physics problems is numerically challenging due to the presence of a wide variety of temporal and spatial scales on which interesting plasma physics phenomena occur throughout the vast domains associated with the large-scale space-weather environment. Numerical solutions of the equations arising in the modelling of these complex flows are computationally intensive and are only feasible on massively parallel computers [1, 2, 3, 4]. Therefore, numerical algorithms capable of efficiently resolving the

solution features of these flows and of reducing the time required to obtain numerical solutions of these problems are an invaluable asset to research communities in the aforementioned fields.

A potential avenue for reducing the computational resource requirements by enhancing solution accuracy for a prescribed mesh resolution, is to develop algorithms that capitalize on recent advances in high-order accurate numerical schemes and in quasi-uniform discretizations of spherical shell geometries. Specifically, for global magnetohydrodynamics (MHD) modelling of space-physics problems, high-order accurate methods have the potential to significantly reduce the number of grid elements required to discretize the vast computational domains associated with celestial bodies and the intervening space, and cubed-sphere grids are attractive for describing simulation domains like the domain between the Sun and the Earth. However, the development of high-order accurate and efficient algorithms for MHD-plasma modelling is challenging due to the intricate nature of the MHD equations which require careful handling of the divergence-free constraint on the magnetic field, due to the coexistence of shocks and smooth small-scale flow features, due to the complexities encountered in the discretization of spherical domains, and due to the difficulty of prescribing high-order boundary conditions (BCs).

In this paper, we develop a three-dimensional (3D) high-order finite-volume (FV) scheme for hyperbolic conservation laws on grids with general hexahedral cells. The method is based on the central essentially non-oscillatory (CENO) method for hyperbolic conservation laws that was proposed by Ivan and Groth for two-dimensional (2D) grids [5], and was originally applied to the Euler and Navier-Stokes equations on multi-block adaptive structured grids [5, 6, 7, 8, 9]. More recently, CENO formulations have been considered on unstructured grids as well [10, 11]. The CENO method is extended in the current work to three dimensions and general hexahedral cells that may have nonplanar faces. This allows us to apply the method to flow simulation on 3D cubed-sphere grids, since cells in cubed-sphere grids have two out of six nonplanar faces. General hexahedral cells are handled by adopting a trilinear description of the nonplanar cell faces, which allows us to compute fluxes, areas and volumes with high-order accuracy by transforming to a reference cubic cell. The resulting high-order 3D finite-volume CENO scheme is applied to MHD flows on cubed-sphere grids by combining it with the generalized Lagrange multiplier (GLM) divergence cleaning method for MHD that was proposed by Dedner *et al.* [12], following our recent work on a 2D CENO method for MHD [13]. The proposed 3D CENO scheme is implemented with fourth-order accuracy in the highly sophisticated parallel and adaptive 3D cubed-sphere grid simulation framework that we presented in [14, 15], resulting in a 3D cubed-sphere grid code for conservation laws that is novel in that it provides solution accuracy with order higher than two uniformly in all three directions. Moreover, our high-order cubed-sphere grid framework has unprecedented capabilities in terms of adaptive refinement and parallel scalability.

High-order numerical discretizations for MHD space-physics flows must properly handle the solenoidal constraint for the magnetic field (i.e.,  $\nabla \cdot \vec{B} = 0$ ) [16] so as to provide stability to the discrete system of differential equations and to avoid unphysical plasma transport effects [17]. They must efficiently provide both solution accuracy and monotonicity even in the presence of large solution gradients and/or discontinuous solutions (e.g. shocks and contacts) and must maintain positivity of flow parameters such as pressure and density throughout the computational domain for solutions varying over many orders of magnitude. These challenging requirements coupled with the additional complexities raised by the treatment of spherical geometric boundaries have limited the widespread application of high-order methods to MHD space-physics flows and thus, the benefits of such accurate discretization methods have yet to be explored for this field.

In recent years, cubed-sphere grids have gained increasing popularity for simulating fluid flow in domains between concentric spheres, first in the area of climate and weather modelling [18, 19, 20, 21, 22, 23, 24], but more recently also in areas like astrophysics [25, 26]. Very recently, Ivan *et al.* [14, 15] have proposed a second-order parallel solution-adaptive computational framework for solving hyperbolic conservation laws on 3D cubed-sphere grids and applied the formulation to the simulation of several magnetized and non-magnetized space-physics problems. In contrast to spherical curvilinear coordinates, cubed-sphere grids (see Fig. 1) are attractive because they offer a nearly uniform covering of the spherical surface, while also providing logically Cartesian grids in each of the six sectors (or panels) of the grid, which can be exploited for efficient implementation. Cubed-sphere grids, however, also pose important numerical challenges due to the grid irregularity and non-trivial connectivity along the boundaries and at the corners of the six sectors of the grid, thus making the formulation of high-order accurate schemes on these grid constructs more difficult.

In spite of these challenges, high-order spatial discretizations on two-dimensional (2D) cubed-sphere grids have been successfully formulated for global atmospheric modelling by Ullrich *et al.* [22] and Chen *et al.* [24]

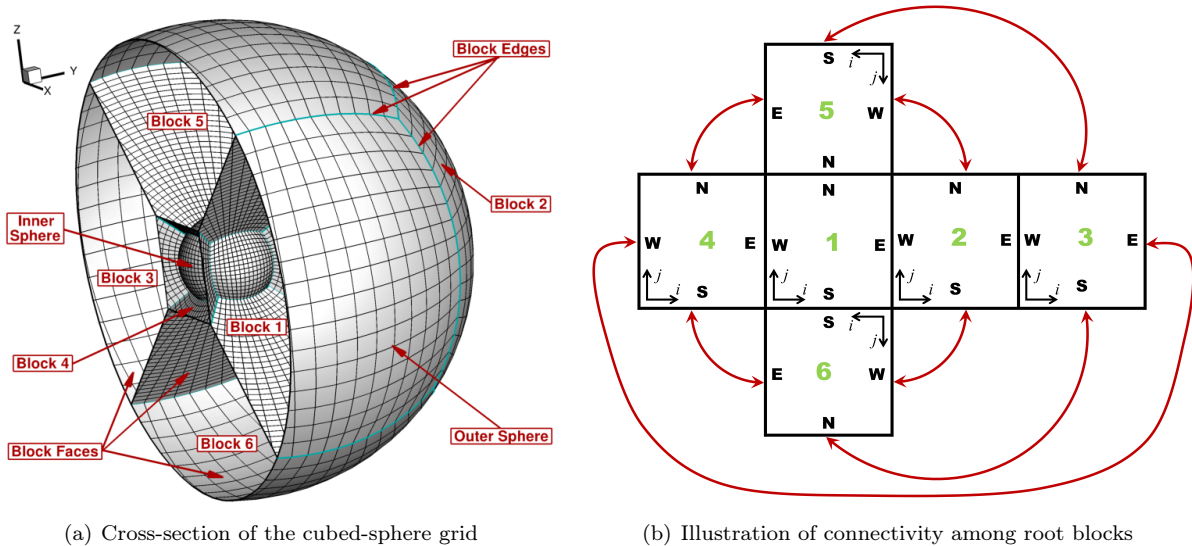


Figure 1: Three-dimensional cubed-sphere grid with six root blocks (corresponding to the six sectors of the grid) and depiction of inter-block connectivity. In our approach, the root blocks can be refined in a block-adaptive way. In panel (b), the block faces are denoted with the initials of the cardinal directions: North (N), East (E), South (S) and West (W).

based on the finite-volume method (FVM), by Nair *et al.* [27] and by Levy *et al.* [28] in the framework of discontinuous Galerkin (DG) and spectral element methods, and by Cheruvu *et al.* [29] using spectral finite-volume transport schemes. Note that all these high-order procedures rely on mapping the governing fluid flow equations on spherical geometry to a Cartesian reference computational domain using non-orthogonal curvilinear coordinates for each sector of the cubed-sphere grid. In other work, Colella *et al.* [30, 31] have developed a high-order FVM on locally-structured grids and performed preliminary studies regarding the high-order interpolation of ghost cell values at the sector boundaries of cubed-sphere grids [30]. It appears that our work is the first to present a numerical scheme on 3D cubed-sphere grids with order of accuracy higher than two uniformly in all three dimensions. Moreover, we maintain high-order accuracy on dynamically adaptive grids and in parallel with good scalability.

In the last two decades, several high-order numerical methods for MHD have been proposed in a quest to formulate accurate, monotone and efficient discretizations that are capable to handle the  $\nabla \cdot \vec{B}$  constraint in a proper way and may be applicable to complex geometries. A variety of approaches have been proposed to handle the  $\nabla \cdot \vec{B}$  constraint. One option is to employ an elliptic correction scheme, called the ‘‘Hodge Projection’’, which essentially projects a vector field onto its solenoidal part [17, 32]. While the elliptic correction scheme maintains solenoidality up to machine accuracy (in the chosen discretization), it requires a Poisson equation to be solved at each hyperbolic step. This approach has several drawbacks such as destroying strict conservation of magnetic field components [33] and difficulties to maintain high-order accuracy and parallelize the solver. As an alternative, Powell [34] proposed a divergence control method in which source terms proportional to the divergence of the magnetic field are introduced to provide a numerically stable way of controlling the errors in the divergence free condition. This modification maintains the hyperbolic character of the MHD equations, but comes at the cost of conservation, and may lead to incorrect jumps for problems with strong discontinuities [16]. A third method to control  $\nabla \cdot \vec{B}$  is the class of schemes that fall under the category of ‘constrained transport’ methods, which preserve the solenoidality of the magnetic field through staggered spatial discretizations [35]. The approach is straightforward to derive and implement for second-order accurate formulations on regular Cartesian grids. It can be extended with second-order accuracy to logically Cartesian grids and to triangular or tetrahedral unstructured grids [36, 37], but extensions beyond second-order [38] and to general polygonal grids are far from trivial. A fourth method is the generalized Lagrange multiplier (GLM) divergence cleaning method proposed by Dedner *et al.* [12].

As in our previous work on a 2D MHD CENO scheme [13], this approach is adopted in the present paper because it is conservative in the physical quantities and can naturally be used on general grids and with high-order accuracy.

This paper is organized as follows. The GLM-MHD formulation is described in Sect. 2. A detailed description of the high-order CENO MHD finite-volume scheme on cubed-sphere grids is provided in Sect. 3. In Sect. 4, the high-order properties of the proposed procedure are demonstrated with grid convergence studies based on analytical solutions for several smooth flows. Furthermore, the robustness against oscillations for flows with shocks is also shown. Concluding remarks are presented in Sect. 5.

## 2 GLM Formulation of Ideal MHD Governing Equations

In this work, the hyperbolic system of ideal MHD equations is solved using a GLM-MHD formulation [12], which couples the divergence constraint,  $\nabla \cdot \vec{B} = 0$ , with the induction equation through the introduction of a new potential variable,  $\psi$ . Thus, the system of conservation laws for which the solution is sought here may be expressed in conservation (or divergence) form as

$$\partial_t \mathbf{U} + \vec{\nabla} \cdot \vec{\mathbf{F}} = \mathbf{S} + \mathbf{Q}, \quad (1)$$

where  $\mathbf{U}$  is the conserved variable solution vector,  $\vec{\mathbf{F}}$  is the system flux dyad, and  $\mathbf{S}$  and  $\mathbf{Q}$  are volumetric source terms. The conserved variable solution vector,  $\mathbf{U}$ , has the form

$$\mathbf{U} = \left[ \rho, \quad \rho \vec{V}, \quad \vec{B}, \quad \rho e, \quad \psi \right]^T, \quad (2)$$

where  $\rho$  is the plasma density,  $\vec{V} = (V_x, V_y, V_z)$  is the velocity,  $\vec{B} = (B_x, B_y, B_z)$  is the magnetic field,  $\rho e$  is the total energy and  $\psi$  is the so-called generalized Lagrange multiplier. The flux dyad,  $\vec{\mathbf{F}}$ , is given by

$$\vec{\mathbf{F}} = \begin{bmatrix} \rho \vec{V} \\ \rho \vec{V} \vec{V} + \left( p + \frac{\vec{B} \cdot \vec{B}}{2} \right) \vec{I} - \vec{B} \vec{B} \\ \vec{V} \vec{B} - \vec{B} \vec{V} + \psi \vec{I} \\ \left( \rho e + p + \frac{\vec{B} \cdot \vec{B}}{2} \right) \vec{V} - (\vec{V} \cdot \vec{B}) \vec{B} \\ c_h^2 \vec{B} \end{bmatrix}. \quad (3)$$

In Eqs. (2) and (3) the specific total plasma energy is  $e = p/(\rho(\gamma - 1)) + V^2/2 + B^2/(2\rho)$ , where  $p$  is the molecular pressure,  $V$  is the magnitude of the fluid velocity, and  $B$  is the magnitude of the magnetic field. The term  $p_B = \frac{\vec{B} \cdot \vec{B}}{2}$  in Eq. (3) is known as the magnetic pressure.

The numerical source term,  $\mathbf{S}$ , is due to the GLM-MHD formulation and given by

$$\mathbf{S} = \left[ 0, \quad \vec{0}, \quad \vec{0}, \quad 0, \quad -\frac{c_h^2}{c_p^2} \psi \right]^T, \quad (4)$$

in which the coefficients  $c_p$  and  $c_h$  control the amount of diffusion in  $\psi$  and the advection speed of the  $\nabla \cdot \vec{B}$ -cleaning mechanism, respectively. Based on the ratio of  $c_h$  and  $c_p$  the transport equation for  $\psi$  in Eqs. (1)-(4) can have a so-called elliptic, parabolic or hyperbolic nature. Moreover, it can be shown [12] that the coefficient  $c_h$  determines how fast the divergence of the magnetic field is advected out of the domain, whereas  $c_p$  controls its dissipation.

Note that Eqs. (1)-(4) represent the non-dimensional scaled form of the MHD equations following from the non-dimensionalization described by, e.g., Powell *et al.* [39] and by Groth *et al.* [2]. The ideal gas equation of state  $p = \rho R T$  is assumed, where  $T$  is the gas temperature and  $R = 1/\gamma$  is the gas constant. For a polytropic gas (thermally and calorically perfect), the ratio of plasma specific heats,  $\gamma$ , is a constant, and the specific heats are given by  $C_v = 1/(\gamma - 1)$  and  $C_p = \gamma/(\gamma - 1)$ . Unless specified otherwise, di-atomic gases are used throughout this paper, which corresponds to  $\gamma = 7/5 = 1.4$ .

The column vector  $\mathbf{Q}$  appearing in Eq. 1 generally represents different volumetric sources arising from the physical modelling of space-physics problems such as sources associated with external gravitational fields. However, in the current work this source term has been used exclusively for constructing an analytical solution to the MHD equations by the method of manufactured solutions [40], as described in Sect. 4.2.2.

### 3 High-Order CENO Scheme for MHD on Cubed-Sphere Grids

High-order solutions of Eqs. (1)-(4) are sought in three spatial dimensions by extending the 2D CENO-GLM high-order MHD scheme proposed in [13] and implementing it into the parallel multi-block solution-adaptive cubed-sphere grid computational framework described in [14, 15]. While the description in this section is for MHD on cubed-sphere grids, the proposed high-order 3D CENO method and our implementation work for general hyperbolic conservation laws and on general grids with hexahedral cells.

Three-dimensional cubed-sphere grids are obtained in our framework by overlaying a sequence of concentric 2D spherical shell grids in the radial direction and forming six three-dimensional sector blocks, each of which is enclosed by the union of four radial and two spherical faces (see Fig. 1). An angularly equidistant mapping [18] is used to generate the initial grids of the six adjoining grid sectors (or panels) that seamlessly cover each of the 2D spheres. In contrast to flows on 2D cubed-sphere grids, for which a curved coordinate system is normally defined on each of the six cubed-sphere sectors, the 3D cubed-sphere grid in principle allows the use of a unique coordinate system (e.g., Cartesian) to discretize the governing conservation laws everywhere in the physical domain, which makes unnecessary the usage of a covariant transformation [18, 22, 41, 42] to map vector fields from the curved coordinate system to the Cartesian system.

However, when using a single global coordinate system the handling of the cubed-sphere discretization in the 3D physical space requires the numerical scheme to be applied on general hexahedral cells. Specifically, each cubed-sphere grid cell in physical space has only the four radial faces as planar quadrilaterals (i.e., all face vertices lay in one plane) whereas the two spherical faces, each defined by four vertices laying on a sphere, are nonplanar. Consequently, to obtain high-order accuracy on these control volumes the nonplanar faces must be carefully treated with regard to all geometric operations affecting the numerical procedure such as flux integration and calculation of geometric properties (e.g., area, volume, centroid, moments etc.). Our proposed solution is to define general hexahedral cells with trilinear faces, which allows us to perform all geometric computations with high-order accuracy by transforming to a reference cubic cell, as discussed in Sect. 3.3. Note that the second-order accurate cubed-sphere discretization employed in our former work [14, 15] used a triangulation-based representation for nonplanar faces which was relatively simple, computationally efficient, and sufficiently accurate to provide second-order accuracy. While the extension to high-order accuracy is still possible based on triangulating the interior nonplanar faces, the use of a standard trilinear face representation [43] has significant advantages when the required number of flux integration points is taken into account and when the water-tightness of inter-cellular faces positioned at mesh resolution changes in an adaptive mesh refinement (AMR) approach is considered (see Sect. 3.4 for details). On the other hand, the usage of trilinear-based hexahedral elements increases the complexity of the implementation and the arithmetic intensity of handling the geometry, especially for high-order accurate schemes, and therefore, careful algorithmic choices must be made to provide relatively efficient high-order implementations.

The hybrid CENO FVM for conservation laws that was proposed by Ivan and Groth [5, 6, 9] is used to discretize the governing equations on the general hexahedral computational grid elements described above. The hybrid CENO procedure uses the multidimensional unlimited  $K$ -exact reconstruction of Barth [44] in smooth regions and reverts to a limited piecewise-linear reconstruction algorithm in regions deemed as non-smooth or under-resolved by a solution smoothness indicator [5], thereby providing monotone solutions near discontinuities. In contrast to other ENO and weighted ENO formulations, the high-order CENO procedure can be extended efficiently and relatively-easily to non-orthogonal 3D grids and large systems of conservation laws due to the use of a fixed multidimensional stencil approach. Taking the same approach as in our previous work on high-order CENO for 2D MHD [13], the 3D MHD CENO algorithm is applied to each solution variable of the modified ideal MHD system Eqs. (1)-(4) to obtain a high-order MHD discretization.

The 3D MHD CENO scheme outlined above is implemented in a 3D multi-block cubed-sphere grid simulation framework [14, 15] which has dynamic adaptive refinement capabilities and high parallel scalability,

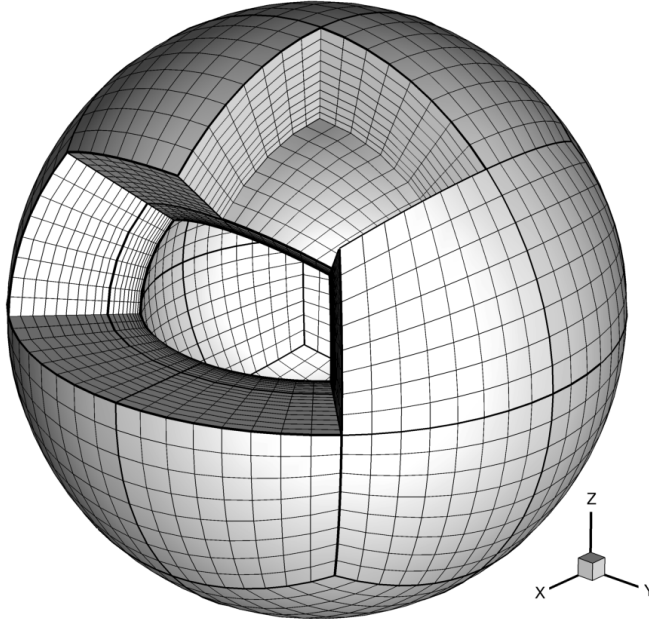


Figure 2: Cubed-sphere grid with 48 equal-size blocks, five of which have been removed. The grid was obtained by dividing each of the initial six blocks into 8 blocks of higher resolution and equal number of cells.

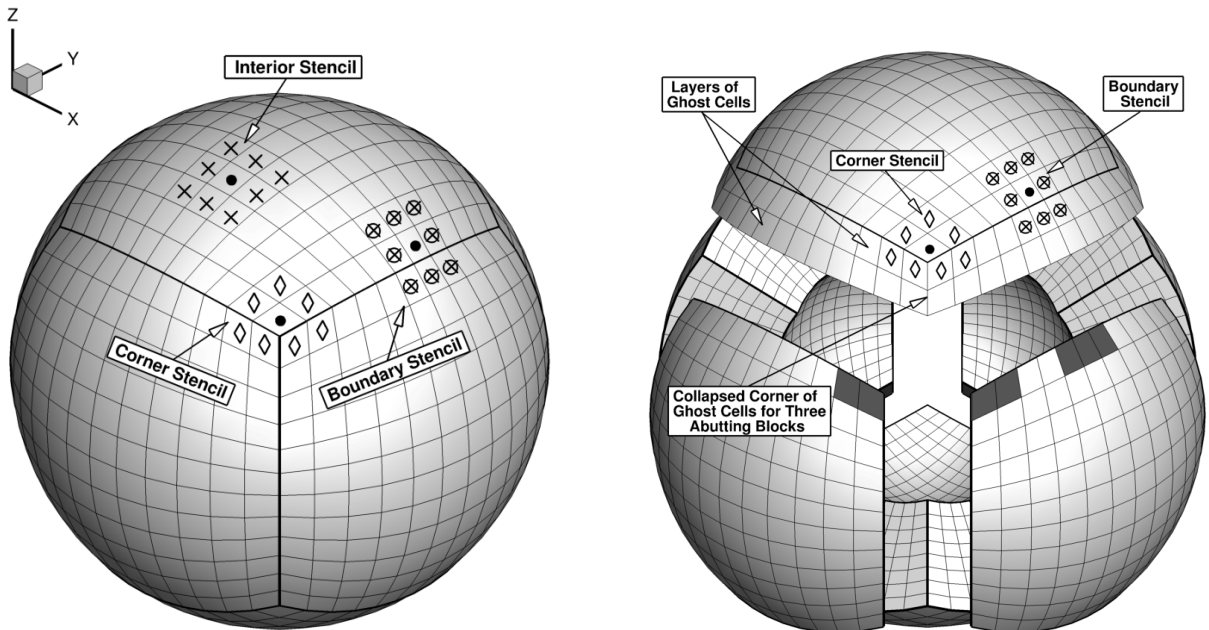
using blocks of equal size. These features have been used in this work to perform the parallel domain partitioning of 3D cubed-sphere grids. Figure 2 illustrates how each of the six initial blocks of a cubed-sphere grid has been divided into 8 blocks of higher mesh-resolution and equal number of cells, thereby generating a final computational cubed-sphere grid with 48 blocks. Thus, parallel high-order numerical simulations with up to 24,576 blocks have been carried out in this work by applying the AMR procedure.

The remainder of this section provides a brief summary of the multi-block cubed-sphere grid followed by a detailed description of the high-order spatial discretization.

### 3.1 Multi-Block Cubed-Sphere Grid with Unstructured Root-Block Connectivity

The 3D cubed-sphere grid simulation framework used in this work is based on a genuine multi-block implementation that was initially developed by Gao and Groth [45, 46] for reacting flows and was later extended and optimized for cubed-sphere grids and space-physics flows by Ivan *et al.* [14, 15]. The computational framework allows for unstructured connectivity between root blocks, which is one of the primary non-standard technical elements that has permitted the handling of cubed-sphere grids. This requirement can be seen by noting in Fig. 1(a) that at the projection of the cube corners (i.e., where the sector edges intersect) three root blocks meet, and as a result, the root-block connectivity of the cubed-sphere multi-block grid is as depicted in Fig. 1(b). Furthermore, the computational framework allows for mesh adaptation accomplished by the dividing and coarsening of appropriate solution blocks, as described in [14, 15, 45, 46]. The preliminary numerical tests in the current work do not take advantage yet of the full dynamic AMR capability of the computational framework, but use only the refinement feature to generate many solution blocks for large-scale parallel simulations.

In the adaptation process a grid hierarchy gets generated from a set of initial (i.e., root) blocks in the form of a sequence of nested grids that can be conveniently tracked with a flexible hierarchical block-tree data structure. The connectivity among blocks that are neighbours in physical space can easily be established using the information stored in the hierarchical octree data structure. The orientation of index axes in adjacent blocks (i.e., the orientation of  $i$ ,  $j$ , and  $k$  indices in the logically Cartesian data structure of neighbouring



(a) Compact view of a cubed-sphere grid and depiction of cells participating in reconstruction stencils in different regions. The data from the cells residing on different blocks than the reconstructed cell is locally reproduced by using overlapping layers of ghost cells, as shown in (b).

(b) Exploded view of the cubed-sphere grid shown in (a) illustrating two ghost cell layers for one block and the actual cells forming the reconstruction stencils. The interior cells marked with shaded grey are the cells from adjacent blocks which have their data duplicated in the ghost cells.

Figure 3: Examples of interior, boundary and corner stencils formed with the first neighbours for different cells of a cubed-sphere mesh with six  $12 \times 12 \times 8$  blocks and a total of 6,912 cells. The cell of which the solution is reconstructed is marked with a  $\bullet$  symbol and the neighbouring cells that are part of the stencil are marked with  $\times$ ,  $\diamond$  and  $\otimes$  symbols for the interior, boundary and corner stencil, respectively.

blocks in physical space) is efficiently stored in compact form as a three-component transformation array. These transformation arrays provide a convenient short-hand notation for the transformation matrices [47, 45, 46] describing the relation between indices of two adjacent blocks, which can be used to exchange solution information between blocks having common interfaces in a general and transparent way. More details about the transformation arrays for the particular case of cubed-sphere grids are given in [15].

The main technical difficulty in applying the block-structured adaptive multi-block concept to cubed-sphere grids is to deal transparently with the unstructured connectivity between adjacent blocks that occurs at sector boundaries and sector corners. A first technical solution is to use block-to-block transformation arrays in the solution procedure, as noted above, to properly compute numerical fluxes across the block boundaries (via the ghost cell and reconstruction mechanisms, see below). However, a second issue arises at sector corners (see Fig. 3): grid cells adjacent to one of the eight sector corners have only seven neighbouring cells (in 2D), while all other cells have 8 neighbours (these neighbours are used in stencils for solution reconstruction and flux calculation, see the next sections). This issue is dealt with in our approach by automatically detecting blocks with such corner cells, and by assigning “collapsed” corner ghost cells to those blocks sharing the relevant corner (as in [46]). In practice, this is implemented by marking these collapsed ghost cells, assigning them dummy values, and not including them in the stencils for reconstruction computation, so grid cells adjacent to sector corners employ reduced stencil sizes. The flexible multidimensional finite-volume reconstruction mechanism of our high-order solution method (see Sect. 3.3) handles this transparently without reducing the local order of accuracy by permitting variable stencil sizes. In our implementation, blocks with collapsed ghost cells are detected from the block connectivity data structure: if no neighbouring block is found in the direction of a block corner the corresponding corner ghost cells are taken to be collapsed.

### 3.2 Semi-Discrete Finite-Volume Formulation

The semi-discrete integral form of the finite-volume formulation applied to Eq. 1 for a hexahedral computational cell  $I(i, j, k)$  of a three-dimensional cubed-sphere grid is given by

$$\frac{d\bar{\mathbf{U}}_{ijk}}{dt} = \frac{1}{V_{ijk}} \left[ - \oint_{\partial\mathcal{V}_{ijk}} \vec{\mathbf{F}} \cdot \vec{n} d\alpha + \iiint_{\mathcal{V}_{ijk}} (\mathbf{S} + \mathbf{Q}) d\mathcal{V} \right], \quad (5)$$

where  $\bar{\mathbf{U}}_{ijk} = \frac{1}{V_{ijk}} \iiint_{\mathcal{V}_{ijk}} \mathbf{U} d\mathcal{V}$  is the solution state of mean conserved variables and  $\partial\mathcal{V}_{ijk}$  is the boundary of the control volume,  $\mathcal{V}_{ijk}$ , of cell  $I$ , which has a volume equal to  $V_{ijk}$ . In Eq. 5 the Gauss divergence theorem has been applied to convert the volumetric flux integral to a surface integration over the boundary  $\partial\mathcal{V}_{ijk}$ . Equation 5 can be further manipulated to get the following semi-discrete form for approximate averages  $\bar{\mathbf{U}}_{ijk}$

$$\frac{d\bar{\mathbf{U}}_{ijk}}{dt} = - \frac{1}{V_{ijk}} \sum_{f=1}^6 \sum_{m=1}^{N_g} (\tilde{\omega} \vec{\mathbf{F}}_{\text{num}} \cdot \vec{n})_{i,j,k,f,m} + (\bar{\mathbf{S}})_{ijk} + (\bar{\mathbf{Q}})_{ijk} = \mathbf{R}_{ijk}(\bar{\mathbf{U}}) \quad (6)$$

by applying a Gauss quadrature integration procedure of variable order of accuracy for the surface integral over the hexahedral cell. The form given by Eq. 6 separates the spatial and temporal discretizations, which essentially reduces the system of partial differential equations (PDEs) to a system of ordinary differential equations (ODEs) in time for each cell. Thus, a high-order numerical approximation to the solution based on Eq. 6 is obtained by computing the discrete spatial residual,  $\mathbf{R}_{ijk}$ , with high-order accuracy and advancing the ODE system in time in an appropriate manner, as discussed in Sect. 3.5.

The numerical flux  $\vec{\mathbf{F}}_{\text{num}} \cdot \vec{n}$  in the normal direction is calculated based on the numerical flux function,  $\vec{\mathbf{F}}_{\text{num}}$ , and the local normal,  $\vec{n}$ , at each of the  $N_g$  Gaussian quadrature points used to integrate the total flux across each face,  $f$ , of the hexahedral cell. Note that according to [43] the quadrature locations at which the fluxes should be evaluated are the images under the trilinear transformation of the Gauss quadrature points in the reference cube, and the Gauss quadrature weights,  $\tilde{\omega}$ , are the weights in the physical space. These weights are obtained from the standard Gaussian weights on the reference cube, multiplied by the local Jacobian of the trilinear transformation, as explained in more detail below. The total number of Gauss integration points,  $N_g$ , at which the numerical flux is evaluated is chosen as the minimum required to preserve the targeted rate of convergence for solution accuracy. High-order evaluation of the residual requires high-order local flux evaluation and accurate integration of the average source terms,  $(\bar{\mathbf{S}})_{ijk}$  and  $(\bar{\mathbf{Q}})_{ijk}$ , which are obtained by providing accurate approximations of the solution variation over the cell following from a polynomial solution reconstruction procedure (see next subsection). In general, an order- $K$  polynomial reconstruction provides an order- $K + 1$  accurate spatial discretization for smooth problems. More details about the residual computation are given in Sect. 3.4.

### 3.3 CENO Reconstruction

High-order solution approximations for the purpose of computing accurate numerical fluxes and volumetric source terms are determined by extending Ivan and Groth's CENO reconstruction procedure [5, 6] for 2D flows to 3D general hexahedral cells and cubed-sphere grids. The CENO reconstruction from [5, 6] is a hybrid procedure that uses the  $K$ -exact piecewise polynomial reconstruction of Barth [44] to provide high-order accuracy in smooth regions and reverts to a limited linear reconstruction procedure to control solution monotonicity only in regions deemed as containing non-smooth and/or under-resolved solution content. Note that a fixed central stencil is used in each of the two reconstruction algorithms, which makes the routine readily applicable to a variety of computational grids in a fairly-straight forward manner. The switching in the hybrid procedure is determined based on a solution smoothness indicator that is computed in each cell for each of the solution variables to determine whether the numerical solution is locally smooth and well-resolved. To control solution positivity, the reconstruction, smoothness analysis and monotonicity enforcement have been applied in this work in the way described in [5, 6, 13], in which the primary choice for performing all these operations is to use the primitive solution variables  $\mathbf{W} = [\rho, \vec{V}, \vec{B}, p, \psi]^T$ . It is

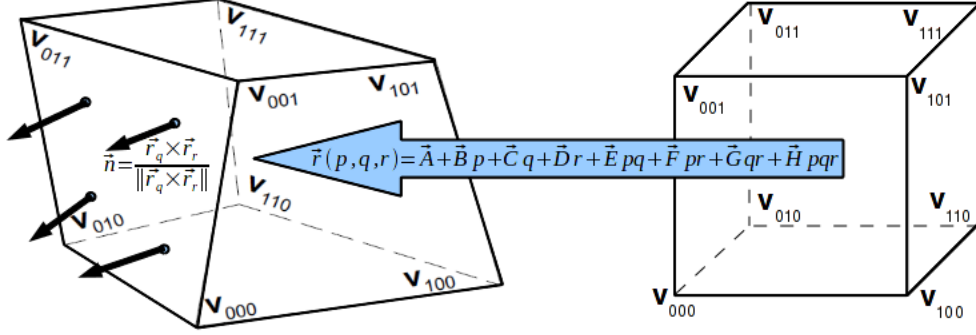


Figure 4: A general hexahedral cell in physical space having faces with nonplanar vertices (left) to which a reference unit cube (right) is mapped by applying a trilinear transformation  $\vec{r}(p, q, r)$ . Four local unit normals are also shown for one face of the general hexahedron.

worth noting that the CENO procedure provides a practical compromise between accuracy, computational efficiency, and robustness that is mostly well-suited for applications having a significant content of smooth solution variations and only a handful of discontinuities.

### 3.3.1 Accurate Integration over General Hexahedral Cells using Trilinear Representations

As previously mentioned, to apply the CENO reconstruction to cubed-sphere grids it is necessary to extend the procedure to hexahedral computational cells that can have faces with nonplanar vertices, as depicted in Fig. 4. A suitable approach is to consider a consistent geometric representation of the general hexahedral cell based on the trilinear transformation

$$\vec{r}(p, q, r) = \vec{A} + \vec{B}p + \vec{C}q + \vec{D}r + \vec{E}pq + \vec{F}pr + \vec{G}qr + \vec{H}pqr, \quad (7)$$

where  $p$ ,  $q$  and  $r$  are Cartesian coordinates in the canonical space of the reference cube and  $\vec{A}$ ,  $\vec{B}$ ,  $\vec{C}$ ,  $\vec{D}$ ,  $\vec{E}$ ,  $\vec{F}$ ,  $\vec{G}$  and  $\vec{H}$  are the transformation vector coefficients that are computed by imposing the one-to-one correspondence between the vertices of the hexahedron and those of the reference cube. Thus, the trilinear transformation,  $\vec{r}(p, q, r)$ , given by Eq. 7 [43, 48] assigns to each point  $(p, q, r)$  in the reference cube an image point  $\vec{X}(x, y, z)$  in the physical space that is part of the hexahedral cell. Consequently, once the transformation coefficients are determined, any local or integrated quantities involving the geometry of the hexahedron (e.g., centroid, volume, face normals, volumetric or face integrals of arbitrary functions, etc.) can be computed by carrying out the required evaluations within the reference cube [43, 49] and not in the distorted hexahedral shape. This approach is extensively used in our CENO method to evaluate all geometry-related quantities required by the solution procedure (see the next sections). The detailed procedure is summarized below for computation of volumetric integrals, in particular the cell volume, and the computations for other quantities like cell centroids, face areas, face integrals, etc., proceed analogously.

The volume of a hexahedral cell is defined by  $V = \iiint_{\mathcal{V}_{ijk}} d\mathcal{v}$ , where  $d\mathcal{v} = dx dy dz$  is the volume element. The more general procedure of evaluating a volumetric integral of a continuous smooth function,  $g(\vec{X})$ , over a control volume  $\mathcal{V}_{ijk}$  is discussed here, which recovers the volume calculation for  $g(\vec{X}) = 1$ . To evaluate the volumetric integral,  $\mathcal{I} = \iiint_{\mathcal{V}_{ijk}} g(\vec{X}) d\mathcal{v}$ , the variables and integration domain are changed to those of the reference unit cube by making use of the trilinear transformation,  $\vec{X} = \vec{r}(p, q, r)$ , and its transformation Jacobian determinant,  $\det \mathbf{J} \equiv \left| \frac{\partial(x, y, z)}{\partial(p, q, r)} \right|$  [43]. Thus, the volumetric integral,  $\mathcal{I}$ , is calculated in the canonical space  $(p, q, r)$  as

$$\mathcal{I} = \int_0^1 \int_0^1 \int_0^1 g(\vec{r}(p, q, r)) \det \mathbf{J} dp dq dr, \quad (8)$$

where the Jacobian  $\det \mathbf{J} = j(p, q, r)$  is also a function of the location.

The triple integral in Eq. 8 is evaluated numerically by applying Gauss-Legendre quadrature integration rules [43, 49] of various accuracy orders depending on the solution accuracy targeted in the computation. For a quadrature rule with  $N_v$  volumetric Gauss points,  $\mathcal{I}$  in Eq.8 is approximated as

$$\mathcal{I} \simeq \sum_{m=1}^{N_v} g(\vec{r}(p_m, q_m, r_m)) (\det \mathbf{J})_m \omega_m = \sum_{m=1}^{N_v} g(\vec{X}_m) \tilde{\omega}_m, \quad (9)$$

where  $\vec{X}_m = \vec{r}(p_m, q_m, r_m)$  and  $\tilde{\omega}_m = (\det \mathbf{J})_m \omega_m$  represent the Gaussian abscissa and weight in the physical space. Note that the abscissa  $\vec{X}_m$  is the trilinear transformation image of the abscissa  $(p_m, q_m, r_m)$  in the reference unit cube and the weight  $\tilde{\omega}_m$  is determined as the product between the local Jacobian and the corresponding Gaussian weight coefficient  $\omega_m$ . Note also that  $(\vec{X}_m, \tilde{\omega}_m)$  depend only on the hexahedral cell geometry and therefore, they can be stored and reused for volumetric integrations involving different  $g(\vec{X})$  functions (e.g., calculation of volume, centroid, geometric moments etc.), and this approach has been taken in the current work to make the implementation more efficient.

For concreteness, calculations based on Eq. 9 of all volumetric geometric properties required by a fourth-order CENO scheme have been performed in this work with a fifth-order Gaussian integration rule derived with three points in each canonical direction (i.e., a  $3 \times 3 \times 3$  product rule [49]) and  $N_v = 27$  volumetric Gauss points. In this rule, the basic abscissae and weights generated for a  $[0, 1]$  domain [50] are  $[0.5, 0.5 \pm 0.3872983346207417]$  and  $[0.4444444444444444, 0.27777777777777763, 0.2777777777777763]$ , respectively.

Although the description of integration rules using the trilinear representation of the hexahedral cell have been illustrated here based on volumetric integrals, it should be clear that a similar approach can be considered for integration over the hexahedral faces. The particular case of the surface flux integration (see Eq. 6) is discussed in Sect. 3.4, including the requirements on the number of face Gauss quadrature points.

### 3.3.2 $K$ -Exact Least-Squares Reconstruction

Following Barth [44], the variation of a solution variable,  $u$ , at any location within the hexahedral computational cell  $I(i, j, k)$  assumes the form

$$u_I^K(\vec{X}) = \sum_{\substack{p_1=0 \\ (p_1+p_2+p_3 \leq K)}}^K \sum_{p_2=0}^K \sum_{p_3=0}^K (x - \bar{x}_I)^{p_1} (y - \bar{y}_I)^{p_2} (z - \bar{z}_I)^{p_3} D_{p_1 p_2 p_3}^K, \quad (10)$$

where  $K$  is the order of the polynomial function,  $\vec{X} = (x, y, z)$  are the coordinates of the position vector at which the solution is sought,  $(\bar{x}_I, \bar{y}_I, \bar{z}_I)$  are the coordinates of the centroid,  $\vec{X}_I$ , of cell  $I(i, j, k)$ , and  $D_{p_1 p_2 p_3}^K$  are high-order polynomial coefficients that will need to be determined for each of the primitive variables for every cell, based on average solution values,  $\bar{u}_{ijk}$ , within the cell and its neighbours. Although Eq.10 allows for arbitrary reconstruction orders, the accuracies targeted in this paper use  $K = 1$  and  $K = 3$  to achieve a second- and fourth-order accurate scheme, respectively. The monotonicity-preserving procedure, which is briefly discussed in Sect. 3.3.3 (for more details see [5, 6, 7, 9, 13]), reduces  $K$  to 1 and applies limiters in regions of the flow that are deemed under-resolved or to contain discontinuities.

The coefficients  $D_{p_1 p_2 p_3}^K$  are determined by solving an overdetermined system of equations in a least-squares sense, fitting the reconstruction polynomial to the averages of the cells that are part of the supporting reconstruction stencil, which consists of the cell  $(i, j, k)$  and a selected number of its neighbouring cells. For a  $K^{th}$ -order polynomial, the number of coefficients  $D_{p_1 p_2 p_3}^K$  is given by  $\mathcal{N}_D = \frac{(K+1)(K+2)(K+3)}{6}$  [6]. Thus, there are four coefficients to be determined for  $K = 1$  or linear reconstruction, ten coefficients for  $K = 2$  or quadratic reconstruction, and twenty coefficients for  $K = 3$  or cubic reconstruction. When determining the coefficients  $D_{p_1 p_2 p_3}^K$ , it is required that the following conditions be satisfied by the reconstruction procedure: 1) the solution reconstruction must reproduce exactly polynomials of degree  $N \leq K$ ; 2) the solution reconstruction must preserve the average value within the computational cell; and 3) the reconstruction procedure must have compact support. Concretely, for a cell  $I(i, j, k)$ , the first condition represents the  $K$ -exactness property

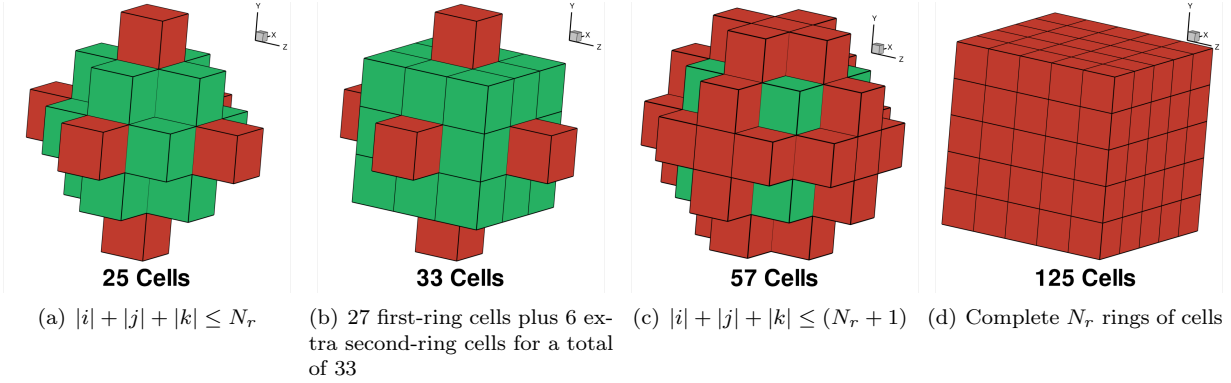


Figure 5: Examples of several central reconstruction stencils for a cell  $(i, j, k)$  ranging in size from 25 to 125 cells that can be used to determine the twenty polynomial coefficients of a cubic reconstruction ( $K = 3$ ). The first-degree neighbours of the cell  $(i, j, k)$  are shown in green whereas dark red is used for the second-degree neighbours. The different stencils are described conveniently using a mathematical relation involving the cell indexes and a selected number of rings,  $N_r$ , that is taken equal to two for this cubic reconstruction case.

[44], the second condition implies that the reconstructed polynomial function should recover exactly the cell-averaged value in cell  $(i, j, k)$ ,

$$\bar{u}_{ijk} = \frac{1}{V_{ijk}} \iiint_{V_{ijk}} u_{ijk}^K(\vec{X}) d\mathfrak{v}, \quad (11)$$

and the third condition refers to the size and locality of the supporting reconstruction stencil [44]. Note that the notation  $u_I^K(\vec{X}) = u_{ijk}^K(\vec{X})$  is used interchangeably.

The minimum size of the compact stencil is determined by the number of required coefficients,  $\mathcal{N}_D$ , but in practice, additional neighbours are included to make the reconstruction more robust to mesh irregularities and solution orientation relative to the grid. Several high-order reconstruction stencils of the types shown in Fig. 5(a)-(d) have been considered for cubic reconstruction ( $K = 3$ ). Preliminary analysis regarding the trade-offs between accuracy and computational efficiency has indicated that the stencil configuration depicted in Fig. 5(b) is an adequate candidate for cubed-sphere grids, and it has been used for all numerical simulations in this work. Thus, the current  $K$ -exact reconstruction scheme uses a fixed central stencil which includes a total of 7 and 33 cells for  $K = 1$  and  $K = 3$ , respectively, for a regular cell, and smaller, but still overdetermined, stencils for cells near the sector boundaries on the cubed-sphere grid.

In the reconstruction step for cell  $I(i, j, k)$  an overdetermined system  $\mathbb{A}\mathbf{D} - \mathbf{B} = 0$  is solved in the least-squares sense, together with the constraint of Eq. 11, which is imposed exactly. Here,  $\mathbf{D}$  is the array of polynomial coefficients,  $D_{p_1 p_2 p_3}^K$ , and the equations  $\mathbb{A}\mathbf{D} - \mathbf{B} = 0$  are given by

$$(\mathbb{A}\mathbf{D} - \mathbf{B})_{\gamma\delta\zeta} = \left( \frac{1}{V_{\gamma\delta\zeta}} \iiint_{V_{\gamma\delta\zeta}} u_{ijk}^K(\vec{X}) d\mathfrak{v} \right) - \bar{u}_{\gamma\delta\zeta} = 0. \quad (12)$$

There is one equation for each cell  $J(\gamma, \delta, \zeta)$  in the stencil of cell  $I(i, j, k)$ . Each equation matches the actual cell average  $\bar{u}_J$  in cell  $J(\gamma, \delta, \zeta)$  with the average over cell  $J(\gamma, \delta, \zeta)$  of the reconstructed polynomial  $u_{ijk}^K(\vec{X})$  for cell  $I(i, j, k)$ . Equation 11 can be enforced analytically by replacing  $u_{ijk}^K$  with Eq. 10 and expressing the first coefficient,  $D_{000}^K$ , as a function of the other  $M = \mathcal{N}_D - 1$  polynomial unknowns as

$$D_{000}^K = \bar{u}_I - \sum_{\substack{p_1=0 \\ (p_1+p_2+p_3 \neq 0)}}^K \sum_{p_2=0}^K \sum_{p_3=0}^K D_{p_1 p_2 p_3}^K (\overline{x^{p_1} y^{p_2} z^{p_3}})_I, \quad (13)$$

where the geometric moment  $(\overline{x^{p_1} y^{p_2} z^{p_3}})_I$  of powers  $(p_1, p_2, p_3)$  is given by

$$(\overline{x^{p_1} y^{p_2} z^{p_3}})_I = \frac{1}{V_I} \iiint_{\mathcal{V}_I} (x - x_I)^{p_1} (y - y_I)^{p_2} (z - z_I)^{p_3} d\mathcal{V}. \quad (14)$$

Substituting  $u_{ijk}^K$  from Eq. 10 in Eq. 12 and using Eq. 13 for  $D_{000}^K$  the following overdetermined linear system for the  $M$  unknowns is obtained

$$\begin{bmatrix} L_1 \\ L_2 \\ \vdots \\ L_J \\ \vdots \\ L_{N_n} \end{bmatrix}_{M \times N_n} \begin{pmatrix} D_{001}^K \\ D_{002}^K \\ \vdots \\ D_{p_1 p_2 p_3} \\ \vdots \\ D_{K00}^K \end{pmatrix}_{N_n \times 1} - \begin{pmatrix} w_1(\bar{u}_1 - \bar{u}_I) \\ w_2(\bar{u}_2 - \bar{u}_I) \\ \vdots \\ w_J(\bar{u}_J - \bar{u}_I) \\ \vdots \\ w_{N_n}(\bar{u}_{N_n} - \bar{u}_I) \end{pmatrix}_{M \times 1} = \begin{pmatrix} 0 \\ 0 \\ \vdots \\ 0 \\ \vdots \\ 0 \end{pmatrix}_{M \times 1} \quad (15)$$

where  $N_n$  is the number of neighbours in the supporting stencil and the generic row  $L_J$  of the matrix  $\mathbb{L}$  for a neighbouring cell  $J(\gamma, \delta, \zeta)$  is given by

$$L_J = \left( w_J \left( \widehat{x^0 y^0 z^1} \right)_{IJ} \quad w_J \left( \widehat{x^0 y^0 z^2} \right)_{IJ} \quad \dots \quad w_J \left( \widehat{x^{p_1} y^{p_2} z^{p_3}} \right)_{IJ} \quad \dots \quad w_J \left( \widehat{x^K y^0 z^0} \right)_{IJ} \right), \quad (16)$$

in which  $w_J$  is a geometric weight specific to each control volume  $J$  which serves the purpose of improving the locality of the reconstruction, becoming especially important for stretched meshes with surface curvature [51]. (In essence, equations corresponding to close-by neighbour cells in the reconstruction stencil get larger weights in the least-squares solution than neighbour cells that are further away.) The matrix coefficients  $\left( \widehat{x^{p_1} y^{p_2} z^{p_3}} \right)_{IJ}$  for the pair of  $I$  and  $J$  cells have the expression

$$\left( \widehat{x^{p_1} y^{p_2} z^{p_3}} \right)_{IJ} = \left( \frac{1}{V_J} \iiint_{\mathcal{V}_J} (x - x_I)^{p_1} (y - y_I)^{p_2} (z - z_I)^{p_3} d\mathcal{V} \right) - (\overline{x^{p_1} y^{p_2} z^{p_3}})_I, \quad (17)$$

where all the quantities  $\left( \widehat{x^{p_1} y^{p_2} z^{p_3}} \right)_{IJ}$  can be efficiently calculated using only the  $(\overline{x^{p_1} y^{p_2} z^{p_3}})$  moments in the way described in [6].

The solution of the overdetermined linear system Eq. 15 can be obtained using QR factorization or by multiplication with the pseudo-inverse of  $\mathbb{L}$  [6, 52]. In each time step, the constrained least-squares reconstruction problem is solved for each cell and for each primitive variable. Matrix  $\mathbb{L}$  depends completely on geometry and is the same for all least-squares problems in a given cell  $(i, j, k)$  and for all time steps, so its inverse can be precomputed and reused to provide a computational speedup (see [5, 6, 9] for details).

### 3.3.3 CENO Smoothness Indicator to Enforce Monotonicity

As in previous CENO formulations [5, 6, 9, 13], in order to control solution monotonicity throughout the computational domain, the high-order  $K$ -exact reconstruction which is deemed non-smooth or under-resolved is reverted to a limited linear reconstruction (i.e.,  $K$ -exact reconstruction with  $K = 1$  combined with a limiting function). In particular, the slope limiter of Venkatakrishnan [53] is used in the limited reconstruction. The smoothness indicator,  $\mathcal{S}$ , used to determine whether a flow variable in cell  $(i, j, k)$  is deemed under-resolved or non-smooth, is computed following the same formulation as in [5]:

$$\mathcal{S} = \frac{\alpha}{\max(1 - \alpha, \epsilon)} \frac{\mathcal{N}_{\text{SOS}} - \mathcal{N}_D}{\mathcal{N}_D - 1}, \quad \alpha = 1 - \frac{\sum_{\gamma} \sum_{\delta} \sum_{\zeta} (u_{\gamma\delta\zeta}^K(\vec{X}_{\gamma\delta\zeta}) - u_{ijk}^K(\vec{X}_{\gamma\delta\zeta}))^2}{\sum_{\gamma} \sum_{\delta} \sum_{\zeta} (u_{\gamma\delta\zeta}^K(\vec{X}_{\gamma\delta\zeta}) - \bar{u}_{ijk})^2}, \quad (18)$$

where the ranges of the indices  $(\gamma, \delta, \zeta)$  are taken to include either the whole or a subset of the supporting reconstruction stencil for cell  $(i, j, k)$ . In Eq. 18,  $\epsilon = 10^{-8}$  is introduced to avoid division by zero and  $N_{\text{SOS}}$  denotes the size of the stencil used for computing the smoothness indicator which in this work was taken equal to seven (i.e., only the cell  $(i, j, k)$  and its first-degree face neighbours were used). The use of the smoothness indicator for the purpose of deciding whether or not to revert a  $K$ -exact reconstruction follows exactly the procedure described in [13], including the use of the same cutoff range values.

### 3.4 High-Order Residual Evaluation for General Hexahedral Cells using Trilinear Representations

As outlined in Sect. 3.2, the high-order accurate numerical computation of the solution residual,  $\mathbf{R}_{ijk}$ , in Eq. 6 requires calculating with high-order accuracy the cell volume  $V_{ijk}$ , the net flux through the boundary of the computational cell  $(i, j, k)$  (i.e., a flux surface integral), the average source term  $(\mathbf{S})_{ijk}$  to the  $\psi$ -update equation (Eq.4), and the average term  $(\mathbf{Q})_{ijk}$  containing any other volumetric sources. High-order accurate approximations to these residual constituents are obtained based on the solution state representation,  $\mathbf{U}_{ijk}^K$ , with a truncation error of  $\mathcal{O}(\Delta x^{K+1})$  for each flow variable and using a high-order quadrature integration of a minimum order to preserve  $\mathcal{O}(\Delta x^{K+1})$ -accuracy. Details related to these procedures are discussed next.

As briefly explained in Sect. 3.2, the high-order accurate calculation of the flux surface integral in Eq. 6 uses a Gauss quadrature rule of  $N_g$  points to approximate the exact flux through each hexahedron face with an accuracy of  $\mathcal{O}(\Delta x^{K+1})$ . For hexahedron faces described with a trilinear representation (see Eq. 7) the selection of  $N_g$  is dictated by the integration rule over quadrilaterals [49] that has an order of integration at least equal to the desired order of solution accuracy. Consequently, the practise adopted here is to use one quadrature point ( $N_g = 1$ ) for second-order schemes ( $K = 1$ ) and four quadrature points ( $N_g = 4$ ) for third- and fourth-order schemes ( $K = 2$  and  $K = 3$ ). To calculate the MHD numerical flux,  $\vec{\mathbf{F}}_{\text{num}} \cdot \vec{n}$ , at each of the  $N_g$  Gauss quadrature points the procedure outlined in [12, 13] is used. Thus, a local Riemann problem with the left and right reconstructed solution states,  $\mathbf{U}_l$  and  $\mathbf{U}_r$ , as initial data is solved at each point by decoupling the equations for  $B_x$  and  $\psi$  from the rest of the system and applying a Lax-Friedrichs numerical flux function to the other seven MHD variables.

Similarly to the integration of flux surface integrals, high-order quadrature rules of an appropriate order can be applied to integrate the volumetric sources and calculate the average source terms in the spatial residual. This approach is used to evaluate the average source term  $(\mathbf{Q})_{ijk}$  by numerically integrating the function  $\mathbf{Q}(\vec{X}, \mathbf{U}_{ijk}^K(\vec{X}))$  over the control volume of cell  $(i, j, k)$  followed by division with  $V_{ijk}$ . The same Gauss quadrature rules used for integrating geometric moments (see Sect. 3.3.2) have been used to integrate this particular source term for the test problems considered in this work. Following Susanto *et al.* [13], a different and more efficient approach is taken for the high-order evaluation of the numerical term introduced by the GLM-MHD formulation,  $(\mathbf{S})_{ijk}$ . In this case, the linear nature of the term allows for analytical integration and direct evaluation as a function of the average value  $\bar{\psi}_{ijk}$  in cell  $(i, j, k)$ , and this formulation is applied in this work. Note that this source term integration is different from the way originally suggested by Dedner *et al.*[12]; a detailed description of our approach is provided in [13].

We use ghost cells to impose boundary conditions, with four layers of ghost cells for the 4th-order method, and two layers for the 2nd-order method. Our current ghost cell boundary implementation is only 2nd-order accurate, except when we impose the exact solution, in which case we determine the ghost cell averages with high accuracy using numerical integration of the exact solution in the ghost cells, which gives us fourth-order accuracy at those boundaries. More general high-order accurate boundary conditions can be obtained by employing a constraint mechanism at the physical boundaries instead of ghost cells. This has not been pursued in the current work, but details on this approach in 2D can be found in [5, 6, 13].

Finally, it is worth emphasizing here the significant advantages of using a trilinear representation instead of triangulating the hexahedral faces. For example, if two triangles were used to represent the nonplanar faces, not only would it have been necessary to have a selection algorithm to choose the face diagonal which defines the two triangles but also, more significantly, the number of points required to calculate the numerical flux [49] would have increased as follows: from one to two (i.e., one for each triangle) for a second-order scheme, and from four to six and to eight for a third- and fourth-order scheme, respectively. These simple facts by themselves demonstrate that employing a trilinear representation over triangulation may

be computationally beneficial. Moreover, the trilinear representation has important advantages when the water-tightness of inter-cellular faces positioned at mesh resolution changes in an adaptive mesh refinement (AMR) approach is considered, because a trilinear face can naturally be divided exactly in four smaller trilinear faces by adding the centroid of the face as an extra grid point. Note that a very desirable property of the trilinear representation is that the centroid of the hexahedral face which is the image of the reference face centroid under the trilinear transformation is also the intersection point of the two face diagonals.

### 3.5 Explicit Temporal Discretization Methods

To obtain steady-state solutions for the problems considered in this work, the coupled system of nonlinear ODEs given by Eq. 6 is solved using multi-stage explicit time-marching schemes [54] in conjunction with global or local time steps obeying the Courant-Friedrichs-Lewy (CFL) stability condition. The source term in the discrete Eq. 6 can in principle influence the stability bound and allowable time step for the ODE system, but a straightforward analysis shows that it does not limit the allowable time step beyond the usual hyperbolic CFL condition for the values of  $c_h$  and  $c_p$  and the grid resolutions used for the test problems included in this paper. This was confirmed in all our numerical tests.

### 3.6 Parallelization with Uniform Treatment of Sector Boundaries and Corners

With the mechanisms of unstructured root-block connectivity and multi-dimensional reconstruction with flexible stencil sizes in place, parallelization on the cubed-sphere grid can be performed in a way that is fully transparent to sector boundaries and corners and remains similar regardless of the solution accuracy of the numerical scheme. The main distinction between different orders of accuracy is in the requirements on the number of ghost cell layers attached to each solution block. As in [15] and the previous work of Groth *et al.*, e.g., [5, 7, 46, 55, 56], an efficient domain partitioning is achieved in our implementation by distributing the active solution blocks equally among available processor cores, with more than one block permitted per processor core. This approach efficiently exploits the self-similar nature of the solution blocks and readily produces an effective load balancing. Inter-processor communication is mainly associated with block interfaces and, for equal-resolution blocks it involves only the exchange of ghost-cell solution values at every stage of the multi-stage time integration procedure. To improve the efficiency of the parallel communication, message passing of the ghost-cell values is performed by consolidating inter-processor messages. Blocks adjacent to grid sector corners feature “collapsed” corner ghost cells, and since there is no neighbour block associated with the collapsed ghost cells in the data structure, messages are not sent for collapsed ghost cells. The combination of this scalable domain partitioning and the effective AMR-based block-multiplication procedure have allowed us to perform efficient parallel high-order calculations on 3D cubed-sphere grids with in excess of 6,000 computing processor cores. No quantitative assessment of the parallel performance has been attempted in this work, although previous strong-scaling performance studies carried out with the second-order formulation of the current cubed-sphere computational framework [15] and with the 2D version of the high-order CENO [6] suggest that the proposed formulation is capable to achieve high-performance levels with good scaling.

## 4 Numerical Results

To demonstrate the capabilities of the proposed high-order CENO scheme described in this paper, numerical results are presented for solution reconstruction of several analytical functions and for three-dimensional flow problems governed by the ideal MHD equations. In grid convergence studies based on an exact solution, the  $L_1$ ,  $L_2$ , and  $L_\infty$  norms of the numerical solution error are computed as follows:

$$L_1 = |E|_1 = \frac{1}{V_T} \sum_{i,j,k} \iiint_{V_{ijk}} \left| u_{ijk}^K(\vec{X}) - f(\vec{X}) \right| d\mathfrak{v}, \quad (19)$$

$$L_2 = |E|_2 = \sqrt{\frac{1}{V_T} \sum_{i,j,k} \iiint_{V_{ijk}} \left[ u_{ijk}^K(\vec{X}) - f(\vec{X}) \right]^2 d\mathfrak{v}}, \quad (20)$$

$$L_\infty = |E|_\infty = \max_{i,j,k} \left( \frac{1}{V_{ijk}} \iiint_{\mathcal{V}_{ijk}} |u_{ijk}^K(\vec{X}) - f(\vec{X})| d\mathcal{V} \right), \quad (21)$$

where  $V_T$  is the total volume of the computational domain,  $f(\vec{X})$  is the exact solution evaluated at point  $\vec{X}$ , and the summation is taken over all the interior computational cells.

## 4.1 Three-Dimensional CENO Reconstructions

Several representative examples of smooth function reconstructions are described now to demonstrate the accuracy of the CENO reconstruction which lies at the core of the proposed high-order FV scheme. These reconstruction tests proceed by first computing highly accurate cell averages for a given function, then using these cell averages to compute high-order polynomial reconstructions in the cells, and finally computing the error between the original function and the polynomial reconstruction over each cell by high-accuracy numerical integration over the cell. The order of convergence of this error as grids are refined measures the order of accuracy of the CENO reconstruction, which determines the order of accuracy of the numerical simulation method. The discrete initial data in these cases is generated by accurately integrating the exact solution over cells to obtain the required cell averages using the integration procedure outlined in Sect. 3.3.1 in combination with an adaptive quadrature approach [57].

### 4.1.1 Reconstruction of Smooth Function on Distorted Meshes for a Rectangular Box Domain

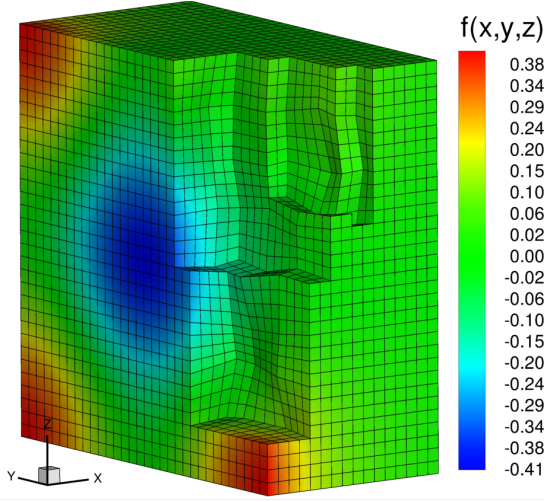
To assess the accuracy of the 3D high-order CENO procedure on meshes containing hexahedral cells with nonplanar faces, reconstructions of the smooth function  $f(x, y, z) = (\cos(\pi(y+1)) - \cos(\pi z))e^{-\pi(x+1)}$  on distorted meshes for a rectangular box domain are compared to the exact solution. The meshes are distorted in such a way that cell faces are nonplanar. Note that  $f(\vec{X})$  represents a combination of trigonometric and exponential terms and also occurs in the expression of the exact solution (as  $B_x$  of the magnetic field) for a 3D magnetohydrostatic problem proposed by Warburton and Karniadakis [58], and for this reason has been selected here. Results for the actual flow problem are discussed in Sect. 4.2.1.

The computational domain used for performing solution reconstruction studies is the rectangular box defined by  $0 < x < 1$  and  $-1 < y, z < 1$ , which is the same domain as that used for the magnetohydrostatic test case (see Sect. 4.2.1). Given the nature of the geometry, Cartesian (possibly stretched) meshes are, in general, sufficient for the discretization of such domains, but to test the accuracy of the CENO reconstruction on general hexahedral cells the interior nodal points have been randomly perturbed as illustrated in Fig. 6(a), giving rise to irregularly-shaped cells with nonplanar faces. The same figure depicts the solution reconstruction obtained on a structured 3D mesh with eight blocks of  $4 \times 8 \times 8$  cells and 2,048 total computational cells using the 4th-order CENO method that is based on a cubic  $K$ -exact reconstruction ( $K=3$ ).

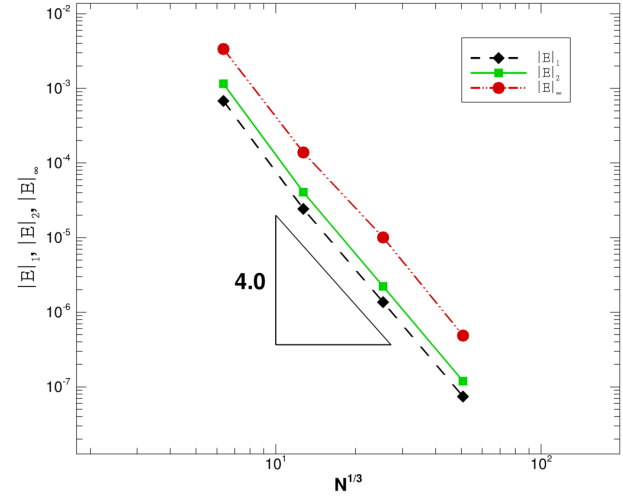
Grid convergence reconstruction studies of the aforementioned  $f(\vec{X})$  function have been carried out with the 4th-order CENO method on a series of meshes generated with the block-based AMR algorithm, of which the initial mesh has one block with  $4 \times 8 \times 8$  cells and 256 total cells and the final mesh obtained after three refinement levels has 512 blocks and 131,072 total computational cells. As shown in Fig. 6(b), the expected theoretical asymptotic convergence rate of the 4th-order accurate method is achieved in all error norms. As the mesh is refined, the slopes of the  $L_1$ -,  $L_2$ -, and  $L_\infty$ -error norms approach -4.176, -4.205 and -4.074, respectively, thereby providing validation for the application of the proposed trilinear-based CENO reconstruction procedure to general hexahedral cells with nonplanar faces.

### 4.1.2 Reconstruction of Radially-Modulated Exponential Function on Cubed-Sphere Grids

To demonstrate the spatial accuracy of the high-order hybrid CENO scheme on 3D cubed-sphere grids, the solution reconstruction of  $f(x, y, z) = (1 - R + R^2)e^{x+y+z}$  on the computational domain defined by two concentric spheres with inner and outer radius  $R_i = 1$  and  $R_o = 3$ , respectively, is considered next. The local radius is denoted by  $R = \sqrt{x^2 + y^2 + z^2}$ . As depicted in Fig. 7(a), this function exhibits a large smooth variation spanning several orders of magnitude that is oriented along the line connecting two diametrically-opposed cubed-sphere corners, where the function maximum and minimum occur. Therefore, this is a good test case for studying how the locally-reduced reconstruction stencil employed by the high-order

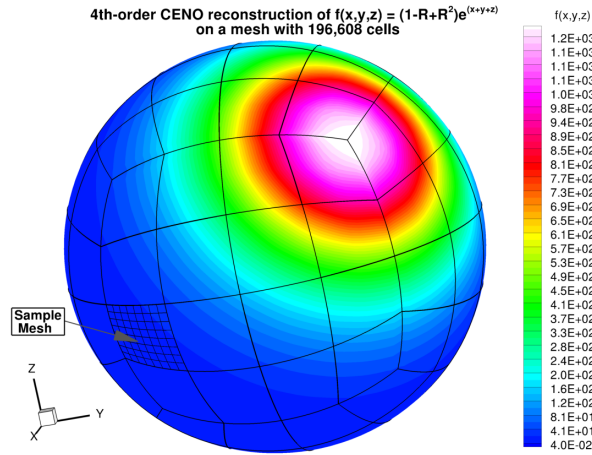


(a) Solution reconstruction obtained on a disturbed mesh with eight blocks of  $4 \times 8 \times 8$  cells and a total of 2,048 cells using a 4th-order CENO reconstruction.

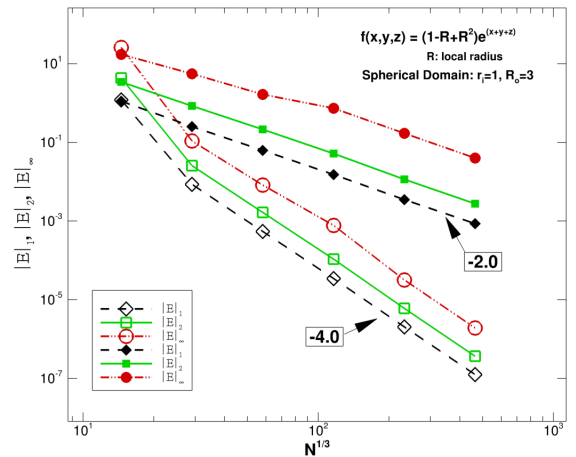


(b) Reconstruction error norms based on the exact solution as a function of the equivalent number of grid points in one-direction.  $N$  is the total number of grid cells.

Figure 6: Fourth-order ( $K = 3$ ) CENO solution reconstruction of  $f(x, y, z) = (\cos(\pi(y + 1)) - \cos(\pi z))e^{-\pi(x+1)}$ . The reconstruction is plotted on a mesh with double resolution to illustrate the high-order nature of the solution reconstruction (left).  $L_1$ -,  $L_2$ -, and  $L_\infty$ -error norms for cubic (4th-order) CENO reconstruction of the function shown in the left panel as a function of the number of computational cells (right).



(a) Depiction of solution reconstruction, block boundaries and the computational mesh of one block.



(b) Comparison of  $L_1$ -,  $L_2$ -, and  $L_\infty$ -error norms for the 2nd- and 4th-order methods vs. the mesh density.

Figure 7: (a) Solution reconstruction of  $f(x, y, z) = (1 - R + R^2)e^{x+y+z}$  on a cubed-sphere grid with  $384 \times 8 \times 8 \times 8$  blocks and 196,608 cells obtained with the 4th-order ( $K=3$ ) CENO method; and (b)  $L_1$ -,  $L_2$ -, and  $L_\infty$ -error norms for a 2nd-order ( $K=1$ ) limited reconstruction and a 4th-order ( $K=3$ ) CENO approach.

reconstruction approach handles solution extrema occurring at the weak singularities of the cubed sphere (where the stencil size is reduced).

In this study, the  $L_1$ ,  $L_2$ , and  $L_\infty$  norms of the reconstruction error associated with the hybrid fourth-order CENO reconstruction are compared against the error norms obtained with a second-order limited  $K$ -exact procedure which is based on a linear reconstruction with a stencil of 26 first-degree neighbours.

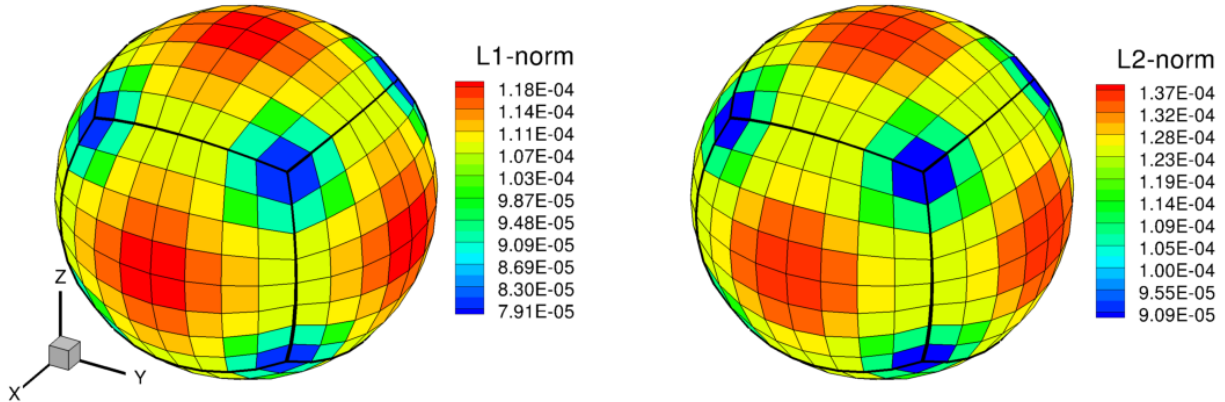


Figure 8: Distribution of average  $L_1$ - and  $L_2$ -error on a sphere of radius  $R=2.6$  obtained for a cubic ( $K=3$ ) CENO reconstruction of  $f(R) = R^{-2.5}$  using a 3D cubed-sphere mesh with radii  $R_i=2$  and  $R_o=3.5$ .

The computational meshes used in this grid convergence study range in size from 3,072 to 100,663,296 cells and have been generated using a block-based AMR procedure in the way described next. In this approach, the initial six blocks of the cubed-sphere grid have been refined successively to generate 48, 384, and 3,072 solution blocks, depending on the targeted number of computational elements. Following this approach the first four meshes in the study have been obtained with blocks of  $8 \times 8 \times 8$  cells, whereas the last two meshes, both with 3,072 blocks, were generated with blocks of  $16 \times 16 \times 16$  and  $32 \times 32 \times 32$  cells, respectively.

The error norms obtained for the two reconstruction procedures on the series of meshes described above are depicted in Fig. 7(b), which shows that both schemes achieve the theoretical convergence accuracy in the asymptotic limit. Moreover, it can be observed by inspecting the convergence plot of the 4th-order reconstruction that the CENO procedure with a cutoff value of 1,500 is able to handle the exponential solution variation both accurately and robustly: on the first mesh containing only  $8 \times 8 \times 8$  cells per grid sector, the function is under-resolved and the high-order CENO procedure avoids creating oscillatory reconstructions by switching to monotonic piecewise linear approximations with larger errors but maintaining monotonicity, whereas on more refined meshes the  $K$ -exact reconstruction is retained everywhere and the reconstruction procedure achieves its theoretical accuracy. Thus, the  $L_1$ ,  $L_2$ , and  $L_\infty$  norms of the solution error in the asymptotic limit are -2.068, -2.121 and -2.101 for the 2nd-order reconstruction method and -4.034, -4.055 and -4.081 for the 4th-order CENO reconstruction. The improved accuracy exhibited by the high-order algorithm translates into significant savings in terms of number of computational cells for a targeted solution error. For example, even to achieve a modest  $L_1=10^{-3}$  solution error, the 2nd-order method requires about 100,663,296 cells, which is more than 500 times the mesh requirements of the high-order method or 196,608 cells, and this factor increases as the error level becomes lower.

#### 4.1.3 Analysis of Reconstruction Error Distribution on Cubed-Sphere Grids

To assess quantitatively the grid influence on solution accuracy for 3D equiangular gnomonic cubed-sphere grids, the high-order CENO reconstruction of the spherically-symmetric function  $f(R)=R^{-2.5}$  is performed on a spherical shell with radii  $R_i=2$  and  $R_o=3.5$ . The computational cubed-sphere grid used in this study consists of six  $8 \times 8 \times 8$  initial blocks and the analysis of error distribution is carried out on a sphere of radius  $R=2.6$  in the interior of the domain to avoid effects from the boundary condition implementation. Note that due to the spherical symmetry of the selected function any non-uniformity in the reconstruction error can only be attributed to local variations in the grid and to the differences in the selection of the reconstruction stencil at sector corners of the cubed-sphere grid.

Figure 8 depicts the spherical distribution of local  $L_1$ - and  $L_2$ -error norms obtained with a cubic ( $K=3$ ) reconstruction on the sphere of radius  $R = 2.6$ . The results show a fairly symmetric error distribution with  $\pm 20\%$  relative variation. These plots show that our approach for obtaining high-order accuracy near the sector boundaries and at sector corners works properly: despite the grid irregularities there and the

use of smaller stencils at sector corners, high-order accuracy is obtained everywhere on the grid. In fact, surprisingly, the error we obtain at the grid sector boundaries and corners is somewhat *smaller* than the error obtained in the interior of the grid sectors. The same behaviour has been confirmed at other radii as well. This indicates that the high-order reconstruction procedure is not affected by the grid non-orthogonality and the reduction in the stencil size near the sector corners, and it suggests that the error is likely mainly dictated by the local mesh spacing: cells near the sector boundaries and corners are smaller than cells in the middle of the sectors, which may explain why the error is smaller there. Consequently, this preliminary analysis indicates that the numerical solution is somewhat better resolved at sector boundaries and corners for the proposed high-order solution reconstruction, but more detailed studies regarding the influence of different stencils and mesh densities, and an analysis for full simulations rather than reconstructions, are required before we can make conclusive statements about the error distribution behaviour on cubed-sphere grids. Nevertheless, it is clear that high-order reconstruction accuracy is obtained everywhere on the cubed-sphere grid, including at sector boundaries and corners, and the numerical results in the next section confirm that global high-order accuracy on the full cubed-sphere grid is also obtained for MHD flow simulations with the proposed high-order CENO approach.

## 4.2 High-Order Results for Magnetized Plasma Flows

A set of three-dimensional numerical results demonstrating the accuracy and capabilities of the proposed high-order CENO finite-volume method on cubed-sphere grids is now described for a range of steady-state flow problems with MHD plasmas.

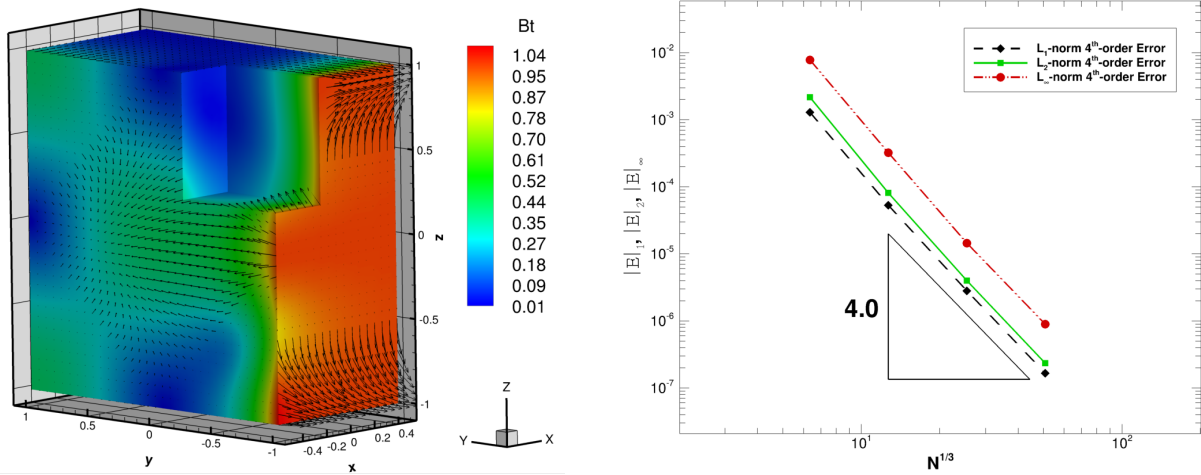
### 4.2.1 Systematic Grid Convergence Studies for a Magnetohydrostatic Test Problem

The first problem to consider is the 3D magnetohydrostatic test case proposed by Warburton and Karniadakis [58] as an extension to the 2D solution derived by Priest [59]. In this particular magnetohydrostatic problem the fluid is static (i.e., has zero velocity) and the magnetic field is irrotational. The domain of the problem is the rectangular box defined by  $0 < x < 1$  and  $-1 < y, z < 1$ . The 3D analytical solution of this flow is given by

$$\begin{aligned}
\rho &= 1, \\
\vec{V} &= \vec{0}, \\
B_x &= (\cos(\pi(y+1)) - \cos(\pi z))e^{-\pi(x+1)}, \\
B_y &= \cos(\pi z)e^{-\pi(y+1)} + \sin(\pi(y+1))e^{-\pi(x+1)}, \\
B_z &= \sin(\pi z)(e^{-\pi(y+1)} - e^{-\pi(x+1)}), \\
p &= 5(\gamma - 1), \\
\psi &= 0,
\end{aligned} \tag{22}$$

where  $\gamma = \frac{5}{3}$  corresponds to monatomic gases. Note that this flow has been used in [58] for performing the accuracy assessment of a high-order discontinuous Galerkin method.

Following [58], this test has been performed as an initial value problem with the exact solution used to provide the initial condition and the values for the Dirichlet boundary conditions for all domain boundaries. Numerical simulations for this problem have been performed with the 4th-order CENO scheme on a series of Cartesian meshes ranging in size from  $4 \times 8 \times 8$  to  $32 \times 64 \times 64$  cells or 256 to 131,072 total cells, respectively, until the solution reached the steady state. The solution to the total magnetic field,  $Bt = \sqrt{B_x^2 + B_y^2 + B_z^2}$ , obtained using the 4th-order ( $K=3$ ) high-order CENO-GLM scheme on a Cartesian mesh with one  $8 \times 16 \times 16$  block and 2,048 total cells is shown in Fig. 9(a). The  $L_1$ ,  $L_2$ , and  $L_\infty$  norms of the error in the  $x$ -component of the magnetic field,  $B_x$ , are given in Fig. 9(b). Error measurements in the other components of the magnetic field,  $B_y$  and  $B_z$ , behave similarly to the error of  $B_x$ , and for the sake of brevity only the error norms based on  $B_x$  are presented. The results of the convergence study in Fig. 9(b) clearly show that the 4th-order theoretical accuracy is achieved by the numerical scheme in all error norms in the asymptotic limit, thereby demonstrating the high-order accuracy of the proposed CENO-GLM formulation for ideal MHD simulations.



(a) Depiction of the magnetic vector field and its magnitude. The top-front corner has been removed for allowing the visualization of the interior solution.

(b) Error norm convergence.

Figure 9: (a) Fourth-order ( $K=3$ ) CENO-GLM results for the total magnetic field,  $Bt$ , for the magnetohydrostatic test case on a Cartesian grid with 2,048 cells; and (b)  $L_1$ ,  $L_2$ , and  $L_\infty$  norms of the error in the  $x$ -component of the magnetic field,  $B_x$ , as a function of mesh density for the 4th-order CENO-GLM scheme.

#### 4.2.2 Systematic Grid Convergence Studies for a MHD Manufactured Solution on Cubed-Sphere Grids

To assess the accuracy of the high-order CENO finite-volume scheme on cubed-sphere grids, we now present convergence studies for a 3D steady-state axi-symmetric exact solution of a MHD plasma on a spherical shell domain flowing outward at supersonic speeds. This test problem has been previously used for accuracy assessment in [14, 15] and represents an adequate three-dimensional test case for solution accuracy on the cubed sphere because the 3D cubed-sphere grid is not axi-symmetric. As far as we know, there are no other non-trivial MHD test problems with an exact solution in a domain between two concentric spheres (except for problems with rather trivial radial 1D solutions, see [15] for examples).

In this test problem, the exact solution is specified using the primitive variables as [14, 15]

$$\mathbf{W}(x, y, z) = \left[ r^{-\frac{5}{2}}, \frac{x}{\sqrt{r}}, \frac{y}{\sqrt{r}}, \frac{z}{\sqrt{r}} + \kappa r^{\frac{5}{2}}, \frac{x}{r^3}, \frac{y}{r^3}, \frac{z}{r^3} + \kappa, r^{-\frac{5}{2}} \right]^T, \quad (23)$$

and the Lagrange multiplier for GLM-MHD is taken  $\psi = 0$ . The exact solution in Eq. 23 gives rise to an analytical residual in Eq.1, which is assigned to the volumetric source term  $\mathbf{Q}$  to balance the equations. This exact solution of a modified set of equations is sometimes called a ‘manufactured solution’ [40]. The analytically-derived source term can be written as [14, 15]

$$\mathbf{Q} = \begin{bmatrix} 0, \\ \frac{1}{2}xr^{-\frac{5}{2}}(r^{-1} - 5r^{-2} - \kappa z), \\ \frac{1}{2}yr^{-\frac{5}{2}}(r^{-1} - 5r^{-2} - \kappa z), \\ \frac{1}{2}zr^{-\frac{5}{2}}(r^{-1} - 5r^{-2} - \kappa z) + \frac{5}{2}r^{-\frac{1}{2}}\kappa(1 + \kappa rz) + \kappa r^{-\frac{1}{2}}, \\ \vec{0}, \\ \frac{1}{2}r^{-2} + \kappa z(3.5r^{-1} + 2\kappa z) + \frac{(\kappa r)^2}{2}(7 + 5\kappa rz) \end{bmatrix}. \quad (24)$$

As suggested in [15], the perturbation parameter is taken as  $\kappa = 0.017$  such that the solution has significant latitudinal variation yet the flow remains supersonic in the whole domain. Note that in this flow the magnetic

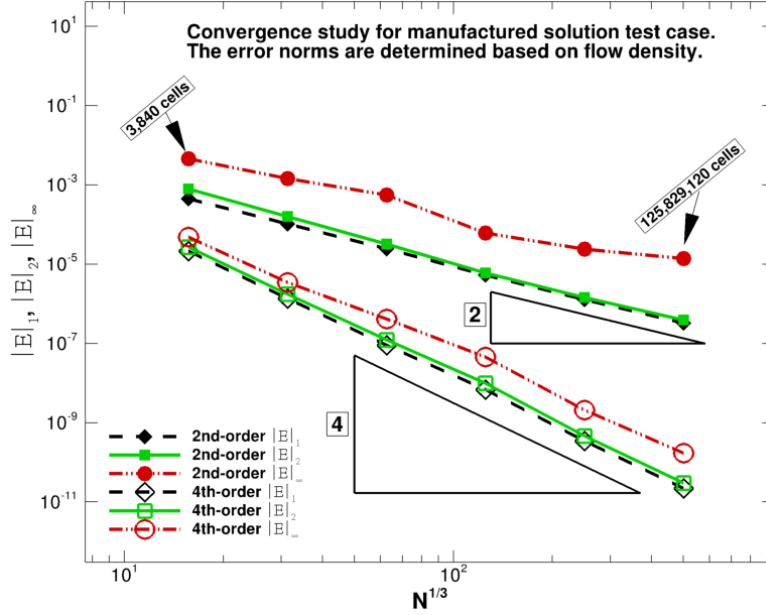


Figure 10: Comparison of  $L_1$ ,  $L_2$ , and  $L_\infty$ -error norms in solution density vs. mesh size obtained with the 2nd- and 4th-order methods for the manufactured MHD solution.

field is irrotational and aligned everywhere with the velocity.

The computational domain used for this convergence study is defined by inner and outer spheres of radius  $R_i=2$  and  $R_o=3.5$ , respectively. To achieve high-order accuracy for this problem, it is necessary to provide a high-order approximation to the average source term,  $(\bar{\mathbf{Q}})_{ijk}$ , in the numerical residual (Eq. 6) by integrating the analytical expression of the source term (Eq. 24) with high-order accuracy, as described in Sect. 3.4. Moreover, high-order boundary conditions must be imposed, which has been achieved in this work by specifying both the inflow and outflow boundary conditions using the exact solution integrated in ghost cells with high-order accuracy to determine the ghost cell averages. These ghost cell averages are used to reconstruct the solution in the ghost cells, and the reconstructed values at the domain boundaries are used together with an interior solution state to solve a local Riemann problem at domain boundaries, in the same way as at interior cell boundaries.

Figure 10 compares the error norms in density obtained with the 2nd-order numerical scheme of [14, 15] with those generated with our 4th-order CENO schemes. A minor difference between the two sets of error norms is that the errors of the 2nd-order scheme have been calculated by comparing the exact and numerical solution at the cell centroid, and not by integration as in Eqs. 19-21. The  $L_1$ ,  $L_2$ , and  $L_\infty$  norms of the error were obtained on a series of grids generated using mesh refinement and ranging in size from six  $8 \times 8 \times 10$  initial blocks to  $24,576 \ 16 \times 16 \times 20$  cubed-sphere blocks, which corresponds to 3,840 and 125,829,120 total cells, respectively. The results depicted in Fig. 10 show that both numerical schemes achieve the theoretical order of accuracy. As the mesh is refined, the slopes of the  $L_1$ ,  $L_2$ , and  $L_\infty$  norms approach in the asymptotic limit -2.06, -2.10 and -2.05, respectively, for the 2nd-order scheme and -4.04, -4.05 and -4.019 for the 4th-order ( $K=3$ ) scheme. However, the improved solution accuracy exhibited by the 4th-order procedure leads to 4th-order error that is as much as 4 orders of magnitude lower than the error generated by the 2nd-order scheme. Thus, the high-order discretization manages to generate significant computational savings compared to the 2nd-order scheme in regard to the number of computational elements required to achieve a target discretization error, which can represent a factor larger than 500, as can be seen in Fig. 10.

These results clearly demonstrate the capability of the proposed high-order scheme to handle MHD flow simulations on spherical shell geometries very accurately. It is clear that global high-order accuracy is obtained on the full cubed-sphere grid with the proposed high-order CENO approach, including at sector boundaries and corners, despite the grid irregularities and reduced stencil sizes there.

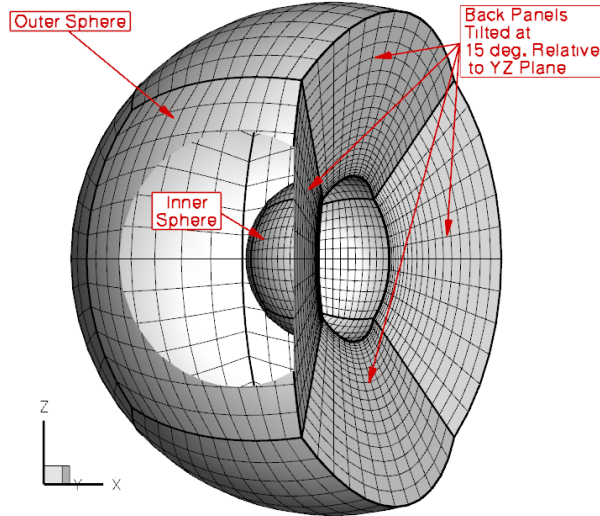


Figure 11: Cubed-sphere grid formed by only five sectors, for simulation on one side of the sphere. A cut in the outer spherical geometry allows a better view of the inner spherical cap.

### 4.2.3 Magnetically Dominated MHD Bow Shock

The robustness of the proposed high-order CENO GLM-MHD scheme on 3D grids with general hexahedral cells is now tested by considering its application to the simulation of 3D MHD bow-shock flows around a perfectly conducting sphere. In particular, the inflow parameters used for this problem have been chosen as in [60] and are  $\rho = 1$ ,  $p = 0.2$ ,  $B_x = 1$ ,  $B_y = 0$ ,  $v_x = 1.4943$  and  $v_y = 0.1307$ , which correspond to an upstream plasma characterized by  $\beta = 2p/B^2 = 0.4$ , an Alfvénic Mach number  $M_{A_x} = 1.49$  along the upstream magnetic field lines and an angle  $\theta_{vB} = 5^\circ$  between the upstream velocity and magnetic vector fields. As shown in [60], this particular upstream configuration corresponds to a MHD “switch-on shock” regime and, thus, gives rise to 3D intermediate shocks and multiple interacting shock fronts.

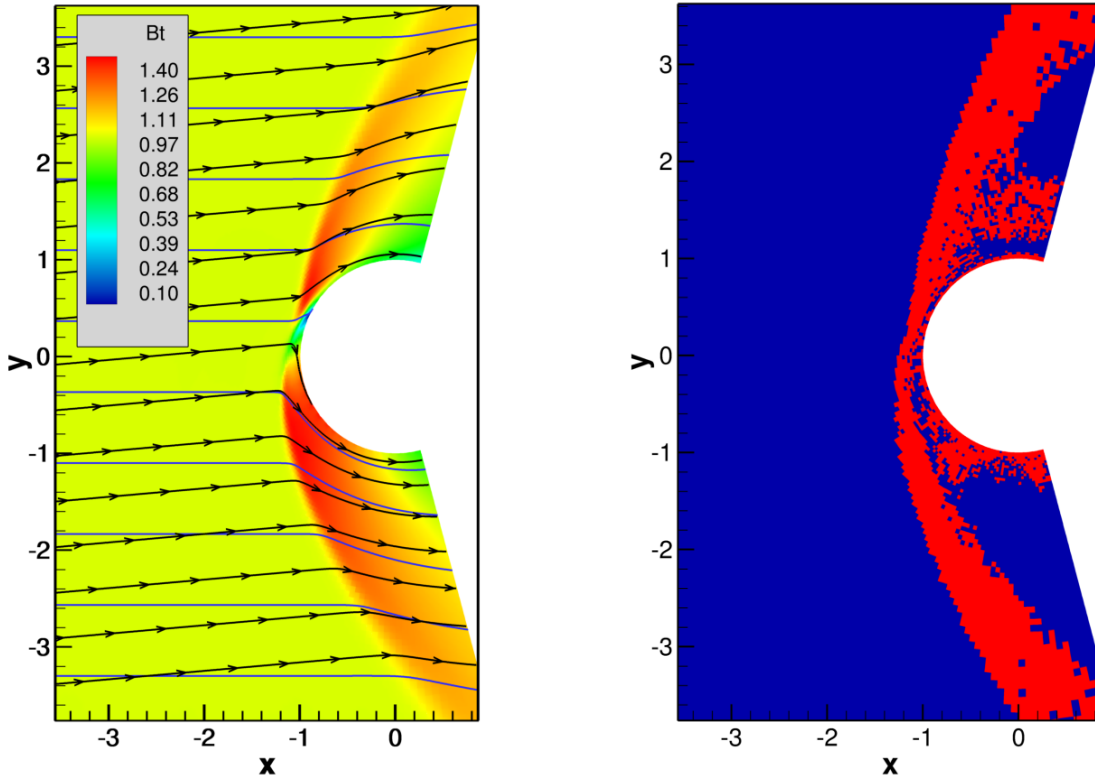
This test case has been studied previously on cubed-sphere grids by Ivan *et al.* [14, 15] using a highly-adapted mesh with 22,693 blocks and 14,523,520 computational cells and a second-order formulation. Similarly to [14, 15], the computational domain used for this problem has the 5-sector configuration shown in Fig. 11, which is defined by two concentric spheres with inner and outer radius  $R_i = 1$  and  $R_o = 8$ , respectively, and the four back panels of the ‘missing sector’ tilted at  $15^\circ$  relative to the Cartesian  $(y, z)$  plane.

A 4th-order CENO scheme with a cutoff of 1,500 is used for the simulation of this challenging flow using a cubed-sphere grid with 320  $12 \times 12 \times 24$  self-similar solution blocks with a total of 1,105,920 computational cells. Reflection boundary conditions are imposed at the inner sphere using a ghost-cell formulation, which can only provide second-order accuracy in this case. Free-stream BCs are applied to the outer boundary and linear extrapolation BCs are implemented for all variables at the back panels of the outer boundary except for  $\psi$ , which is set to zero (see the discussion in [13] and [61] for more details on boundary conditions for  $\psi$ ).

Total magnetic field contours are shown in Fig. 12(a), on top of which are superimposed the streamlines (black colour) and also the magnetic field lines (blue colour). Consistently with the findings in [60], a secondary shock front is observed following the leading bow-shock front, in agreement with the magnetically dominated upstream conditions.

Figure 12(b) shows the effect of the smoothness indicator, illustrating the non-uniformity in the order of polynomial reconstruction (with the cells shown as blue representing high-order reconstruction, whereas limiters are applied to cells tagged as red). As desired, the flow is flagged as non-smooth in the vicinity of the shocks. Note that there are also flagged cells close to the obstacle, but this is due to the 2nd-order boundary conditions. In future work, this will be remedied by implementing 4th-order accurate wall boundary conditions using the constraint mechanism described in [5, 6, 13].

The contours in Fig. 12(a) close to the shocks do not show any indication of spurious oscillations, and more detailed investigation of the results (not shown) confirm that no spurious oscillations are generated



(a) Total magnetic field contour lines. Black lines represent velocity streamlines, and blue lines are magnetic field lines.

(b) CENO switching criterion. Cells coloured in red represent regions of limited linear reconstruction.

Figure 12: (a) Fourth-order CENO-GLM result for the total magnetic field,  $Bt$ , on the Cartesian  $(x, y)$  plane at  $z=0$  obtained on a mesh with 1,105,920 cells for the magnetically dominated bow-shock problem; and (b) corresponding regions in which the CENO scheme uses unlimited cubic (blue) and limited linear (red) reconstruction for the  $x$ -direction magnetic field,  $B_x$ .

at the shocks. This illustrates that the 4th-order CENO scheme succeeds in producing 4th-order accurate results in smooth parts of the flow while preserving monotonicity at shocks on cubed-sphere grids with general hexahedral elements, confirming our findings for the 2D 4th-order MHD CENO scheme in [13].

## 5 Conclusion

This paper has presented a 3D high-order CENO finite-volume scheme for hyperbolic conservation laws on grids with general hexahedral cells. The method is based on the CENO scheme for hyperbolic conservation laws that has been proposed by Ivan and Groth for 2D grids in [5, 6, 15]. The main technical difficulty in extending the high-order 2D CENO scheme to general hexahedral cells in 3D is to properly treat hexahedral cells that may have nonplanar cell faces. In our approach, general hexahedral cells are handled by adopting a trilinear description of the nonplanar cell faces, which allows for the computation of fluxes, areas and volumes with high-order accuracy by transforming to a reference unit cube. The resulting high-order CENO method has been applied to fluid flow problems on 3D cubed-sphere grids, which have hexahedral cells with two out of six nonplanar faces. The 3D CENO scheme has been used to simulate MHD flows by combining it with the generalized Lagrange multiplier (GLM) divergence cleaning method for MHD that was proposed by Dedner et al. [12], following our recent work on a 2D CENO method for MHD [13]. The proposed 3D CENO

scheme has been implemented with fourth-order accuracy in the highly sophisticated parallel and adaptive 3D cubed-sphere grid simulation framework that we have presented in [14, 15]. Detailed numerical results that demonstrate uniform fourth-order convergence for smooth flows and robustness against oscillations for flows with shocks have been discussed. We have also investigated error distributions and have found that for our approach the numerical error at the corners and boundaries of the six cubed-sphere grid sectors are not larger than in the interior of the sectors. Our approach maintains high-order accuracy at sector corners by employing multi-dimensional reconstruction on overdetermined stencils that can have varying size and do not need to be grid-aligned. To our knowledge, the proposed 3D cubed-sphere grid simulation framework for conservation laws is the first scheme for 3D cubed-sphere grids with an order of accuracy higher than two in all three space dimensions. Moreover, our framework maintains high-order accuracy on adaptive grids and in parallel.

Future research will involve development of accurate high-order boundary conditions using the constraint mechanism, the full connection of the high-order procedure with the dynamic block-based AMR framework, the coupling with an effective parallel implicit algorithm (see, for example, the methods of Northrup and Groth [62, 63]), and application of the high-order computational framework to complex space-physics problems.

## Acknowledgements

This work was supported by CSA (Canadian Space Agency) CGSM Contract No. 9F007-080157/001/ST. Computations were performed on the GPC supercomputer at the SciNet HPC Consortium and on the facilities of the Shared Hierarchical Academic Research Computing Network (SHARCNET:www.sharcnet.ca). The SciNet and SHARCNET consortia are funded by: the Canada Foundation for Innovation under the auspices of Compute/Calcul Canada; the Government of Ontario; Ontario Research Fund - Research Excellence; and the member institutions of the consortia.

## References

- [1] W. B. Manchester IV, A. Vourlidis, G. Tóth, N. Lugaz, I. I. Roussev, I. V. Sokolov, T. I. Gombosi, D. L. De Zeeuw, and M. Opher. Three-dimensional MHD simulation of the 2003 October 28 coronal mass ejection: comparison with LASCO coronagraph observations. *Astrophys. J.*, 684:1448–1460, 2008.
- [2] C. P. T. Groth, D. L. De Zeeuw, T. I. Gombosi, and K. G. Powell. Global three-dimensional MHD simulation of a space weather event: CME formation, interplanetary propagation, and interaction with the magnetosphere. *J. Geophys. Res.*, 105(A11):25,053–25,078, 2000.
- [3] T. I. Gombosi, K. G. Powell, D. L. De Zeeuw, C. R. Clauer, K. C. Hansen, W. B. Manchester, A. J. Ridley, I. I. Roussev, I. V. Sokolov, Q. F. Stout, and G. Tóth. Solution-adaptive magnetohydrodynamics for space plasmas: Sun-to-Earth simulations. *Comp. Sci. & Eng.*, 6(2):14–35, 2004.
- [4] C. Jacobs. *Magnetohydrodynamic modelling of the solar wind and coronal mass ejections*. PhD thesis, University of Leuven, October 2007.
- [5] L. Ivan and C. P. T. Groth. High-order Central ENO finite-volume scheme with adaptive mesh refinement. Paper 2007-4323, AIAA, June 2007.
- [6] L. Ivan. *Development of High-Order CENO Finite-Volume Schemes with Block-Based Adaptive Mesh Refinement*. PhD thesis, University of Toronto, October 2010.
- [7] L. Ivan and C. P. T. Groth. High-order solution-adaptive central essentially non-oscillatory (CENO) method for viscous flows. Paper 2011-0367, AIAA, January 2011.
- [8] Z.J. Zhang and C. P. T. Groth. Parallel high-order anisotropic block-based adaptive mesh refinement finite-volume scheme. Paper 2011-3695, AIAA, June 2011.
- [9] L. Ivan and C. P. T. Groth. High-order solution adaptive central essentially non-oscillatory (CENO) method for viscous flows. 2012. Submitted.
- [10] S. D. McDonald, M. R. J. Charest, and C. P. T. Groth. High-order CENO finite-volume schemes for multi-block unstructured mesh. Paper 2011-3854, AIAA, June 2011.
- [11] M. R. J. Charest, C. P. T. Groth, and P. Q. Gauthier. High-order CENO finite-volume scheme for low-

- speed viscous flows on three-dimensional unstructured mesh. In *Proceedings of the 7th International Conference on Computational Fluid Dynamics, Hawaii, USA, July 9–13, 2012*. Paper ICCFD7-1002.
- [12] A. Dedner, F. Kemm, D. Kroner, C-D. Munz, T. Schitzer, and M. Wesenberg. Hyperbolic divergence cleaning for the MHD equations. *J. Comput. Phys.*, 175:645–673, 2002.
- [13] A. Susanto, L. Ivan, H. De Sterck, and C. P. T. Groth. High-order central ENO finite-volume scheme for ideal MHD. 2012. Submitted.
- [14] L. Ivan, H. De Sterck, S. A. Northrup, and C. P. T. Groth. Three-dimensional MHD on cubed-sphere grids: Parallel solution-adaptive simulation framework. Paper 2011-3382, AIAA, June 2011.
- [15] L. Ivan, H. De Sterck, S. A. Northrup, and C. P. T. Groth. Hyperbolic conservation laws on three-dimensional cubed-sphere grids: A parallel solution-adaptive simulation framework. 2012. Submitted.
- [16] G. Tóth. The  $\nabla \cdot \mathbf{B} = 0$  constraint in shock-capturing magnetohydrodynamics codes. *J. Comput. Phys.*, 161(2):605–652, 2000.
- [17] J. U. Brackbill and D. C. Barnes. The effect of nonzero  $\nabla \cdot \mathbf{B}$  on the numerical solution of the magnetohydrodynamic equations. *J. Comput. Phys.*, 35:426–430, 1980.
- [18] C. Ronchi, R. Iacono, and P. S. Paolucci. The "cubed sphere": A new method for the solution of partial differential equations in spherical geometry. *J. Comput. Phys.*, 124:93–114, 1996.
- [19] A. Adcroft, J.-M. Campin, C. Hill, and J. Marshall. Implementation of an atmosphere-ocean general circulation model on the expanded spherical cube. *Mon. Weather Rev.*, 132:2845–2863, 2004.
- [20] W. M. Putman and S.-J. Lin. Finite-volume transport on various cubed-sphere grids. *J. Comput. Phys.*, 227:55–78, 2007.
- [21] A. St-Cyr, C. Jablonowski, J. M. Dennis, H. M. Tufo, and S. J. Thomas. A comparison of two shallow-water models with nonconforming adaptive grids. *Mon. Weather Rev.*, 136:1898–1922, 2008.
- [22] Paul A. Ullrich, Christiane Jablonowski, and Bram van Leer. High-order finite-volume methods for the shallow-water equations on the sphere. *J. Comput. Phys.*, 229(17):6104 – 6134, 2010. DOI: 10.1016/j.jcp.2010.04.044.
- [23] C. Chen and F. Xiao. Shallow water model on cubed-sphere by multi-moment finite volume method. *J. Comput. Phys.*, 227:5019–5044, 2008.
- [24] C. G. Chen, F. Xiao, X. L. Li, and Y. Yang. A multi-moment transport model on cubed-sphere grid. *Int. J. Numer. Meth. Fluids*, 67:1993–2014, 2011.
- [25] A. V. Koldoba, M. M. Romanova, G. V. Ustyugova, and R. V. E. Lovelace. Three-dimensional magnetohydrodynamic simulations of accretion to an inclined rotator: the "cubed sphere" method. *Astrophys. J.*, 576:L53–L56, 2002.
- [26] P. C. Fragile, C. C. Lindner, P. Anninos, and J. D. Salmonson. Application of the cubed-sphere grid to tilted black hole accretion disks. *Astrophys. J.*, 691:482–494, 2009.
- [27] R. D. Nair, S. J. Thomas, and R. D. Loft. A discontinuous Galerkin transport scheme on the cubed sphere. *Mon. Weather Rev.*, 133:814–828, 2005.
- [28] M. N. Levy, R. D. Nair, and H. M. Tufo. High-order Galerkin methods for scalable global atmospheric models. *Comput. & Geos.*, 33:1022–1035, 2007.
- [29] V. Cheruvu, R. D. Nair, and H. M. Tufo. A spectral finite volume transport scheme on the cubed-sphere. *Appl. Numer. Math.*, 57:1021–1032, 2007.
- [30] P. Colella, M.R. Dorr, J.A.F. Hittinger, P. McCorquodale, and D. F. Martin. High-order finite-volume methods on locally-structured grids. Paper, Numerical Modeling of Space Plasma Flows: ASTRONUM-2008, 2008.
- [31] P. Colella, M.R. Dorr, J.A.F. Hittinger, and D.F. Martin. High-order, finite-volume methods in mapped coordinates. *J. Comput. Phys.*, 230(8):2952 – 2976, 2011.
- [32] A. J. Chorin. A numerical method for solving incompressible viscous flow problems. *Journal of Computational Physics*, 2:12–26, 1967.
- [33] D. S. Balsara and J. Kim. A comparison between divergence-cleaning and staggered-mesh formulations for numerical magnetohydrodynamics. *Astrophys. J.*, 602:1079–1090, 2004.
- [34] K. G. Powell. An approximate Riemann solver for magnetohydrodynamics (that works in more than one dimension). Report 94-24, ICASE, July 1994.
- [35] C. R. Evans and J. F. Hawley. Simulation of magnetohydrodynamic flows: A constrained transport method. *Astrophys. J.*, 332:659, 1988.
- [36] H. De Sterck. Multi-dimensional upwind constrained transport on unstructured grids for 'shallow water'

- magnetohydrodynamics. *AIAA*, 2001-2623, 2001.
- [37] D. S. Balsara. Second-order accurate schemes for magnetohydrodynamics with divergence-free reconstruction. *The Astrophysical Journal Supplement Series*, 151:149–184, 2004.
- [38] D. S. Balsara. Divergence-free reconstruction of magnetic fields and WENO schemes for magnetohydrodynamics. *J. Comput. Phys.*, 228:5040–5056, 2009.
- [39] K. G. Powell, P. L. Roe, T. J. Linde, T. I. Gombosi, and D. L. De Zeeuw. A solution-adaptive upwind scheme for ideal magnetohydrodynamics. *J. Comput. Phys.*, 154:284–309, 1999.
- [40] P. J. Roache. *Verification and Validation in Computational Science and Engineering*. Hermosa Publisher, New Mexico, 1998.
- [41] R. Sadourny. Conservative finite-difference approximations of the primitive equations on quasi-uniform spherical grids. *Mon. Weather Rev.*, 100(2):136–144, 1972.
- [42] P. A. Ullrich. *Atmospheric Modeling with High-Order Finite-Volume Methods*. PhD thesis, University of Michigan, 2011.
- [43] O.C. Zienkiewicz and R.L. Taylor. *The Finite Element Method*, volume 1. Butterworth-Heinemann, fifth edition, 2000.
- [44] T. J. Barth. Recent developments in high order k-exact reconstruction on unstructured meshes. Paper 93-0668, AIAA, January 1993.
- [45] X. Gao. *A Parallel Solution-Adaptive Method for Turbulent Non-Premixed Combusting Flows*. PhD thesis, University of Toronto, 2008.
- [46] X. Gao and C. P. T. Groth. A parallel solution-adaptive method for three-dimensional turbulent non-premixed combusting flows. *J. Comput. Phys.*, 229:3250–3275, 2010.
- [47] NASA. CGNS, CFD general notation system. Retrieved from <<http://www.grc.nasa.gov/www/cgns/>> (Accessed June 26, 2012).
- [48] J. F. Thompson, Z. U. A. Warsi, and C. W. Mastin. *Numerical Grid Generation—Foundations and Applications*. North-Holland, New York, 1985.
- [49] C. A. Felippa. A compendium of FEM integration formulas for symbolic work. *Eng. Comput.*, 21(8):867–890, 2004.
- [50] W. H. Press, S. A. Teukolsky, W. T. Vetterling, and B. P. Flannery. *Numerical Recipes. The Art of Scientific Computing 3rd-Edition*. Cambridge University Press, New York, 2007.
- [51] D. J. Mavriplis. Revisiting the least-squares procedure for gradient reconstruction on unstructured meshes. Paper 2003-3986, AIAA, June 2003.
- [52] C.L. Lawson and R.J. Hanson. *Solving least squares problems*. Prentice-Hall, INC, 1974.
- [53] V. Venkatakrisnan. On the accuracy of limiters and convergence to steady state solutions. Paper 93-0880, AIAA, January 1993.
- [54] B. van Leer, C. H. Tai, and K. G. Powell. Design of optimally-smoothing multi-stage schemes for the Euler equations. Paper 89-1933-CP, AIAA, June 1989.
- [55] J. S. Sachdev, C. P. T. Groth, and J. J. Gottlieb. A parallel solution-adaptive scheme for predicting multi-phase core flows in solid propellant rocket motors. *Int. J. Comput. Fluid Dyn.*, 19(2), 2005.
- [56] X. Gao and C. P. T. Groth. A parallel adaptive mesh refinement algorithm for predicting turbulent non-premixed combusting flows. *Int. J. Comput. Fluid Dyn.*, 20(5):349–357, 2006.
- [57] W. Gander and W. Gautschi. Adaptive quadrature – revisited. *BIT*, 40:84–101, 2000.
- [58] T. C. Warburton and G. E. Karniadakis. A discontinuous Galerkin method for the viscous MHD equations. *J. Comput. Phys.*, 152:608–641, 1999.
- [59] E. R. Priest. *Solar Magneto-Hydrodynamics*. Reidel Publishing, Boston, 1982.
- [60] H. De Sterck and S. Poedts. Intermediate shocks in three-dimensional magnetohydrodynamic bow-shock flows with multiple interacting shock fronts. *Phys. Rev. Lett.*, 84(24):5524–5527, 2000.
- [61] M. S. Yalim, D. Vanden Abeele, A. Lani, T. Quintino, and H. Deconinck. A finite volume implicit time integration method for solving the equations of ideal magnetohydrodynamics for the hyperbolic divergence cleaning method. *J. Comput. Phys.*, 230:6136–6154, 2011.
- [62] S. A. Northrup and C. P. T. Groth. Prediction of unsteady laminar flames using a parallel implicit adaptive mesh refinement algorithm. In *Proceedings of the 6th U.S. National Combustion Meeting*, May 2009.
- [63] S. A. Northrup and C. P. T. Groth. Parallel implicit AMR scheme for unsteady reactive flows. In *Proceedings of the 18th Annual Conference of the CFD Society of Canada, London, Canada*, May 2010.